Studying away side jet fragmentation using x_{E} distributions in proton-proton collisions at $\sqrt{s} = 2.76$ TeV taken by ALICE

Mikko Kervinen

Master's thesis

University of Jyväskylä

Department of Physics

Supervisor: Sami Räsänen

January 25, 2013

Abstract

Two-particle correlations are a useful method to study high energy particle collisions exhibiting a jet structure. It examines the relations of a selected trigger particle and other particles in the collision called associated particles. At the leading order, partons are produced in back-to-back pairs in the transverse plane due to a momentum conservation. Hadronization of these partons leads into (ideal) di-jet events. This implies that if we can select a trigger hadron from one jet, then we should find correlated particles of the back-to-back jet from the opposite (away) side of the trigger particle. In this study we concentrate on away side jet properties by studying the distribution of the longitudinal component of associated particle momentum with respect to the trigger particle (x_{E}). The distribution comprised of charged hadron data from proton-proton collisions at $\sqrt{s} = 2.76$ TeV measured by ALICE.

The measured x_{E} distributions had notable background contributions from particles not originating from the high energy scattering of partons that is being studied. This study presents a Monte Carlo -based method to remove this combinatorial background from the measurements.

The resulting signal distributions exhibited behaviour that gave support for earlier conclusion by PHENIX Collaboration at RHIC, stating that the shape of the x_{E} distributions measured in (charged) hadron-hadron correlations does not follow the fragmentation function.

Preliminary results from $p + p$ collisions at $\sqrt{s} = 7$ TeV from ALICE suggested that the the slope of the x_{E} distribution at the tail region is sensitive to the trigger momentum fraction $z_{\mathrm{t}} = p_{\mathrm{Tt}}/\hat{p}_{\mathrm{Tt}}$ where p_{Tt} and $\hat{p}_{\mathrm{Tt}}$ are the transverse momenta of the trigger hadron and parton, respectively. I repeated this analysis for $\sqrt{s} = 2.76$ TeV data. Obtained results are similar to those previously found in ALICE at $\sqrt{s} = 7$ TeV and by that strengthen the conclusions from earlier analyses.

One of the experimental challenges is the trigger bias which shows such that the mean momentum fraction in the hadronization process grows from its inclusive value in the near side when the trigger condition is posed. Also, in the case that there are phenomena that causes imbalance between trans-

verse momenta of the partons that initiate the di-jet, then the trigger is more likely the parton with the higher initial momentum. Such imbalance can be quantified with the parameter $\langle \hat{x}_{\mathrm{h}} \rangle$ that measures the ratio between average momenta of the near side and away side partons. I will discuss a model that relates this parameter kinematically to the x_{E} distributions. It turns out that ALICE data gives $\langle \hat{x}_{\mathrm{h}} \rangle < 1$ clearly in the experimental error bars and hence the imbalance is observed.

Tiivistelmä

Kaksihiukkaskorrelaatiot ovat hyvä tapa tutkia jettejä, eli kollimoituja hiukkassuihkuja, joita syntyy suurenergisissä hadroni-hadroni törmäyksissä. Niissä tarkastellaan valitun triggeri-hiukkasen ja muiden törmäyksessä syntyneiden liittohiukkasten (associated particle) välisiä korrelaatioita. Johtavassa kertaluvussa kovassa sironnassa syntyy kaksi partonia, jotka ovat vastakkaissuuntaiset poikittaistasossa (transverse plane) liikemäärän säilymisen nojalla. Näiden partonien hadronisoituminen johtaa (ideaalisiin) di-jetti tapahtumiin. Jos pystymme valitsemaan toisesta jetistä trigger-hiukkasen, niin voimme odottaa vastakkaisen jetin (away side jet) hadronisaatioista tulevan trigger-hiukkasen kanssa korreloituja liittohiukkasia. Tässä työssä pyritään selvittämään triggerin vastakkaisen jetin ominaisuuksia tutkimalla liittohiukkasten liikemäärän pitkittäiskomponentin ja trigger-hiukkasen liikemäärän suhteen (x_{E}) jakaumia. Jakaumat oli koostettu ALICE-kokeessa suoritetuissa $\sqrt{s} = 2.76$ TeV:n protoni-protoni –törmäyksissä mitatuista varatuista hadroneista.

Mitatut x_{E}-jakaumat sisältävät kombinatorisen taustan, joka syntyy korreloitumattomista hiukkaspareista, jotka eivät liity kovaan sirontaan törmäysprosessissa. Työssä esitellään Monte Carlo -menetelmä kombinatorisen tausta poistamikseksi mittaustuloksista.

Saadut tulokset antoivat tukea RHIC -törmäyttimen PHENIX -kokeen tuloksille, joiden perusteella hadroni-hadroni korrelaatioissa mitattujen x_{E}-jakaumien muoto ei seuraa fragmentaatiofunktiota.

ALICEn preliminääriset tulokset $\sqrt{s} = 7$ TeV:n $p + p$-törmäyksistä viittaavat siihen, että x_{E}-jakauman hännän eksponentiaalinen vaimeneminen mittaa havaitun trigger hadronin ja sironneen partonien poikittaisliikemäärien suhdetta z_{t}:tä. Suoritin vastaavan analyysin $\sqrt{s} = 2.76$ TeV:n datalle ja saadut tulokset olivat sopusoinnussa aikaisempien havaintojen kanssa.

Yksi kokeellisen tutkimuksen haasteista on, että trigger-ehdosta seuraa trigger-puolen keskimääräisen liikemääräosuuden kasvu sen inklusiivisesta arvosta, mistä käytetään nimitystä trigger bias. On olemassa prosesseja, kuten $2 \to 3$ sironnat, jotka rikkovat jettien liikemäärien ideaalisen tasapainon.

Trigger biaksen seurauksena trigger hadroni tulee todennäköisemmin jetistä, jonka syntyy suurenergisemmän partonin hadronisaatioissa. Tätä epätasapainoa voidaan tutkia parametrillä $\langle \hat{x}_{\mathrm{h}} \rangle$ joka mittaa trigger ja assosioidun partonin keskimääräisten liikemäärien suhdetta. Tutkielmassani käsittelen kinemaattista mallia jossa tämä parametri liitetään x_{E}-jakaumiin. Tutkimani ALICE-datan perusteella $\langle \hat{x}_{\mathrm{h}} \rangle < 1$ selvästi virherajojen sisällä ja täten havaitsin epätasapainon.

Contents

1 Introduction

The Large Hadron Collider (LHC) [1] at CERN, the European Laboratory for Nuclear Research, is at the forefront of experimental particle physics. It is located near Geneva at the border of Switzerland and France. It's designed to collide proton beams up to a center of mass energy of $\sqrt{s} = 14$ TeV and at a luminosity of $10^{34}\text{cm}^{-2}\text{s}^{-1}$. It's also capable of colliding heavy ions.

There are four major experiments along the LHC ring: ATLAS [2], CMS [3], ALICE (A Large Ion Collider Experiment) [4] and LHCb [5]. Of these ALICE is a dedicated heavy ion experiment, its main goal being to study quark-gluon plasma. ALICE is optimized for heavy ion collisions, however it is also able to measure proton-proton ($p+p$) collisions. Its sensitivity at low momentum and excellent particle identification allows some measurements that are not possible in the other LHC experiments.

The underlying theory behind contemporary particle physics is called the standard model [6]. It states that all matter consists of combinations of quarks and leptons and that the interactions of these constituents can be described by three fundamental forces: electromagnetic, weak and strong nuclear interactions. In the following we will concentrate mainly on the strong interaction and quarks.

The interactions between quarks are mediated by gluons. Both quarks and gluons have a color charge which is analogous to the electromagnetic charge in Quantum Electrodynamics (QED) [7], except that there are three color charges as opposed to two. The interactions of color charged particles is described by a quantum field theory called Quantum Chromodynamics (QCD) [8]. Similarly to QED, perturbation theory can be used to calculate scattering cross sections of QCD processes.

The relevant features of the QCD, w.r.t. this analysis, are the confinement of quarks and asymptotic freedom. Confinement of quarks means that the force between quarks increases with with distance that prevents a free quark or gluon to propagate macroscopic distances in free space. In the constituent quark model the simplest colorless bound states are quark–anti-quark pairs called mesons and three quark states called baryons. Together, mesons and

baryons, i.e. bound quark systems, are called hadrons.

Asymptotic freedom means that at small distances or at high energies the force between quarks weakens. At high energies otherwise confined quarks can thus behave as though they're free. Confinement and asymptotic freedom are features that are of great significance when dealing with high-energy collisions.

1.1 High-energy particle collisions

The process where a colored quark or a gluon turns into colorless final state hadrons is called hadronization [9]. At high energies, the conservation of momentum collimates the created hadrons into narrow sprays of particles, called jets [10]. In the following, I will concentrate mainly on dijet events which exhibit two nearly back-to-back jets.

The first experimental evidence for jets was seen at the Stanford Positron Electron Asymmetric Rings (SPEAR) collider at SLAC [11, 12]. SPEAR observed that the final state hadrons were not isotropically distributed, instead, showing a jet-structure. Further e^+e^- collision experiments paved the way for contemporary jet physics. Scatterings of electrons and positrons were favoured as they provided a very clean environment to observe jets since the initial state is annihilated and jets emerge clearly from a very low background.

The possibility of observing jets in hadron collisions were debated at first. It was not certain if the constituents of hadrons could interact in a way to create jets. They were finally observed at the Intersecting Storage Rings (ISR) at CERN [13, 14]. In this thesis I will concentrate on hadron-hadron collisions.

The difficulty with hadronic collisions is the internal structure of the hadrons, and the initial and final state interactions of the associated color fields. The situation is made even more difficult since the internal structure of hadrons is much more complicated than just the constituent quarks of the bound state. Instead, the structure of a hadron includes so-called valence quarks, sea quarks and gluons. The valence quarks account for the quantum numbers of the hadron, while the sea quarks are quark-antiquark pairs

constantly being created and annihilated within the hadron.

In the parton model [15] hadrons are collections of quasi-free, pointlike particles called partons. They're identified as gluons and quarks, though they're not identical to constituent quarks.

1.2 Collinear factorization

In the framework of collinear factorization hadron collisions are divided into three stages:

- The initial state interactions, which are long-distance interactions and thus cannot be calculated using perturbative QCD (pQCD).
- The partonic scattering which can be calculated using pQCD provided the process has high enough energy, i.e. is "hard".
- The hadronization of partonic states produced in the hard scattering. This is the least understood stage and, as with the initial state interactions, pQCD is not applicable.

This division is often called the factorization theorem [10].

In calculating cross sections, the initial state interactions and hadronization are accounted for by probability functions. The cross section of a semi-inclusive interaction a+b -> H + X, where X is "anything at all" (i.e. not measured/specified), has the form [16]

$$d\sigma^{ab\to H+X} = \sum_{i,j,k} f_i^a(x_1) \otimes f_j^b(x_2) \otimes \hat{\sigma}^{ij\to k+x}(x_1, x_2) \otimes D_k^H(z, Q^2). \quad (1)$$

In this equation the sum runs through all possible partonic processes that can lead into semi-inclusive production of H in scattering of hadrons a and b. Above $\hat{\sigma}^{ij\to k+x}$ is the QCD cross section of the partonic hard scattering, functions $f_i^a(x_1)$ and $f_j^b(x_2)$ are called parton distribution functions (PDF) and $D_k^H(z, Q^2)$ is called a fragmentation function (FF). The PDF $f_i^a(x_1)$ gives the probability that parton i carries momentum fraction x_1 of hadron a. The FF $D_k^H(z, Q^2)$ describes the hadronization process. It gives the probability

that that parton k will fragment into hadron H which will carry a fraction $0 < z \leq 1$ of the momentum of the original parton at given scale Q^2.

As we're unable to calculate PDFs and fragmentation functions from theory, they are parametrized and the fit parameters are tuned by making a global analysis to all available experimental data. It is assumed that both sets of functions are universal, which means that when measured in one process they can be used in another. PDFs are most accurately determined from deep inelastic scatterings of electrons on protons whereas fragmentation functions are determined from electron-positron scatterings. It should be noted that universality of these functions is a conjecture, but the experimental data has proven it to be a good assumption.

1.3 Fragmentation function

In the following, I will describe in detail how fragmentation functions are acquired from data. As an example I will examine the set of fragmentation functions made by Kniehl, Kramer and Pötter (KKP) [17].

Fragmentation functions are extracted from e^-e^+ scatterings because then we need not to consider PDFs in Eq. (1), but the kinematics of the initial state is simple. To calculate the FF we need to examine the inclusive production of a hadron h in the annihilation process

$$e^+e^- \to (\gamma, Z) \to h + X. \tag{2}$$

The process of calculating FFs at scale Q^2 starts by acquiring it at energy scale Q_0^2 from data, and then using the so called Alterelli-Parisi QCD evolution equations to bring them into scale Q^2 [18].

The key observable is the scaled-momentum distribution normalized to the total hadronic cross section $(1/\sigma_{tot})d\sigma^h/dx$, where $x = 2E_h/\sqrt{s}$ is the energy fraction of the outgoing hadron h. This we cannot derive from theory. Instead it can be obtained by a convolution of the cross sections $(d\sigma_a/dx)(x, \mu^2, Q^2)$ of the relevant partonic subprocesses $e^-e^+ \to a + X$, and

the FFs $D_a^h(x, Q^2, \mu^2)$ giving

$$\frac{1}{\sigma_{tot}}\frac{d\sigma_h}{dx} = \sum_a \int_x^1 \frac{dz}{z} D_a^h(z, Q^2) \frac{1}{\sigma_{tot}} \frac{d\sigma_a}{dy}\left(\frac{x}{z}, \mu^2, M_f^2\right). \tag{3}$$

Here the sum runs through all active partons, μ is the renormalization scale and Q is the fragmentation scale. I will not go into more detail on the partonic subprocesses or the renormalization procedure, other than that in principle we can calculate them perturbatively to arbitrary precision. At the moment, the analysis is performed in Next-to-Leading-Order (NLO). More details on the partonic subprocesses can be found in [19].

The FFs are acquired through a fit of Eq. (3) into data from experiments. In order to do this we need to parametrize the FFs. In the KKP set the following parametrization was used:

$$D_a^h(x, Q_0^2) = N x^\alpha (1-x)^\beta, \tag{4}$$

where N, α and β are independent fit parameters. Eq. (3) is fit into several sets of data simultaneously. This means that if one would consider two flavours from two data sets with different final state hadrons, one would have $3 \times 2 \times 2 = 12$ free parameters in the fit.

The KKP fragmentation functions [17] were calculated from $K^\pm$, $\pi^\pm$ and $p/\overline{p}$ data collected by the TPC, DELPHI, OPAL, ALEPH and SLD experiments. The fits included charged-hadron data from TPC at $\sqrt{s} = 29.0$ GeV [20], and DELPHI [21], ALEPH [22] and SLD [23] at $\sqrt{s} = 91.2$ GeV. In addition to this the OPAL [24] and ALEPH [25] experiments supplied gluon-tagged data. The charged hadron data distinguished fragmentation of quark flavours in four cases i) u, d and s quarks, ii) b quark only, iii) c quark only and iv) all five quark flavours.

The number of fit parameters can somewhat be reduced by imposing

iso-spin symmetry based on constituent quark content

$$
\begin{aligned}
D_u^{\pi^\pm}(x,Q_0^2) &= D_d^{\pi^\pm}(x,Q_0^2), \\
D_u^{K^\pm}(x,Q_0^2) &= D_s^{K^\pm}(x,Q_0^2), \\
D_u^{p/\overline{p}}(x,Q_0^2) &= 2D_d^{p/\overline{p}}(x,Q_0^2).
\end{aligned}
\tag{5}
$$

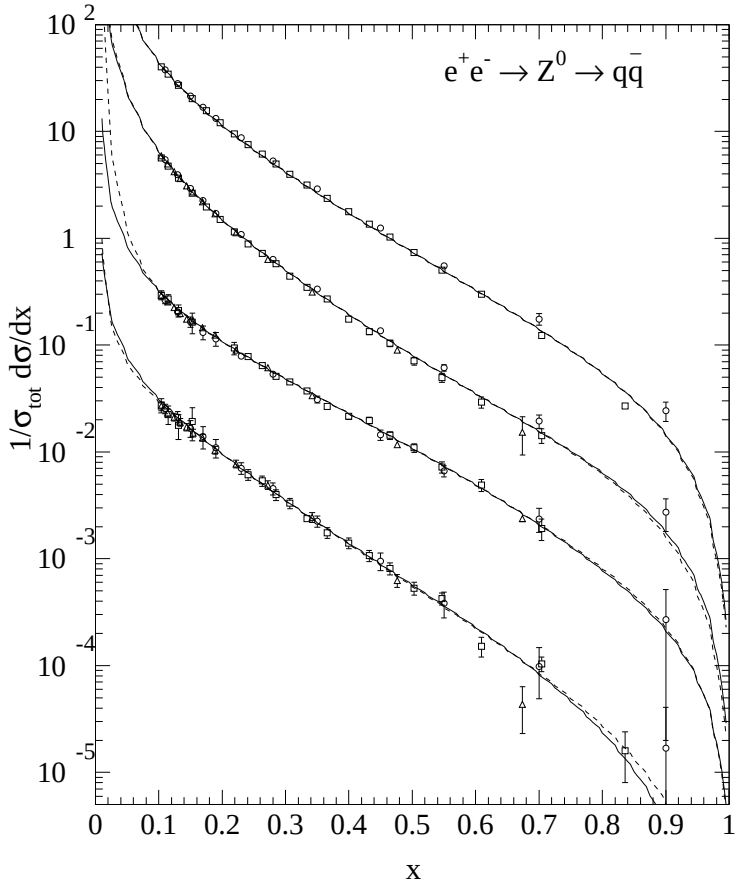

Figure 1: An example of the fits made by KKP [17]. Normalized differential cross section of inclusive hadron production at $\sqrt{s} = 91.2$ GeV as a function of x. The LO (dashed lines) and NLO (solid lines) fit results are compared with data from ALEPH (triangles), DELPHI (circles), and SLD (squares). The upmost, second, third, and lowest curves refer to charged hadrons, $\pi^\pm$, $K^\pm$, and $p/\overline{p}$, respectively. Each pair of curves is rescaled relative to the nearest upper one by a factor of 1/5.

Eventually the fits made by KKP had a total of 46 free parameters [17]. The starting scale Q_0 was in the case of u, d and s quarks and gluons $Q_0 = \sqrt{2}$ GeV with c quarks $Q_0 = 2.9788$ GeV and with b quarks $Q_0 = 9.46037$ GeV. The fits were made in the interval $0.1 \leq x \leq 1$, where the small x was cut to exclude events in the nonperturbative region. An example of the fits made by KKP is illustrated in Fig. 1. To get a sense of what order of magnitude the values of N, α and β can have, I present examples of the b quark fragmentation functions acquired by KKP:

$$\begin{aligned} D_b^{\pi^\pm}(x, Q_0^2) &= 0.259 x^{-1.99}(1-x)^{3.53}, \\ D_b^{K^\pm}(x, Q_0^2) &= 1.32 x^{-0.884}(1-x)^{6.15}, \\ D_b^{p/\overline{p}}(x, Q_0^2) &= 24.3 x^{0.579}(1-x)^{12.1}. \end{aligned} \tag{6}$$

These FFs are also illustrated in Fig. 2

Although $e^- e^+$ collisions provide the cleanest environment to determine FFs in experiments, one still wishes to study them also e.g. in proton-proton

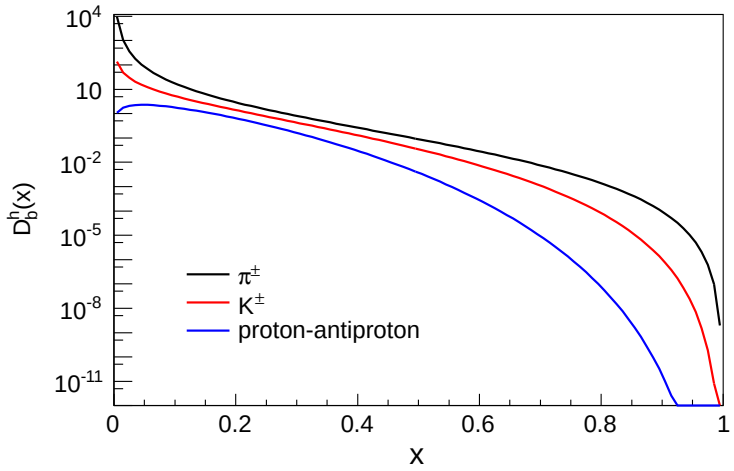

Figure 2: Examples of fragmentation functions from describing the fragmentation of a b quark to $\pi^\pm$ (black), $K^\pm$ (red) and $p/\overline{p}$ (blue).

physics. One would, for example, like to test the assumption of universality of fragmentation functions made above. Also, in heavy ion collisions one seeks to see modification of the fragmentation functions [26]. Therefore, finding a proton-proton reference measurement would be very important. Especially the latter goal motivates to make the analysis using two-particle correlation since that framework is easier to work with also at the heavy ion collisions where the jet reconstruction is a formidable task [27].

2 Two-particle correlations in $p + p$ collisions

In this section I will review some of the historical background of two-particle correlations in high energy particle collisions. The center of the review will be the momentum fraction x_{E} and what it tells us about the fragmentation process. I will start with the results of the CERN-Columbia-Oxford-Rockefeller collaboration (CCOR), move on to the Pioneering High Energy Nuclear Interaction Experiment (PHENIX) at the Relativistic Heavy Ion Collider (RHIC) and finish off with the currently on-going analysis of ALICE at CERN. I will start by discussing briefly two-particle correlations in general.

2.1 Azimuthal two-particle correlations

While in full jet reconstruction jets are studied event-by-event basis, with two particle correlations one studies their properties statistically [28]. A trigger particle with some given characteristics is sought event-by-event. If such is found, then all other particles that fulfil other given conditions, referred to as associated particles, are correlated with the trigger. These criteria depend on what one aims to study. Here, I choose that the trigger particle is always the leading charged hadron, i.e. the particle with highest $p_{\mathrm{T}} = |\vec{p_{\mathrm{T}}}|$, if it belongs in some of the pre-defined trigger bins. Here, I consider all other charged hadrons with $p_{\mathrm{Tmin}} < p_{\mathrm{T}} < p_{\mathrm{Tt}} = p_{\mathrm{T}}^{trigger}$ as associated particles that will be correlated with the trigger. At the end, one sums up all events and typically presents the results normalized to number of fired triggers in the studied data set.

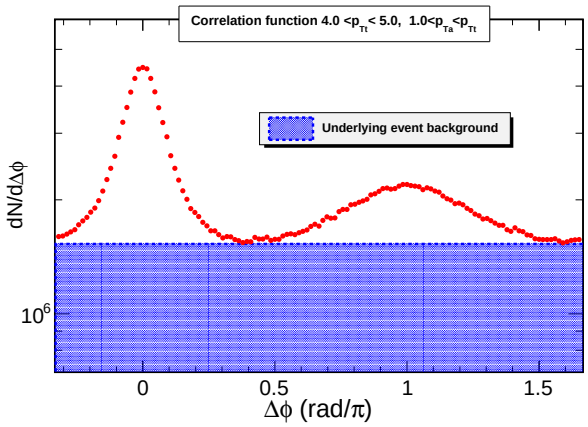

Figure 3: Leading particle charged hadron azimuthal correlation function from ALICE proton-proton collisions at $\sqrt{s} = 7$ TeV, showing the underlying event background. The underlying event pedestal, under the peaks shown in blue, was evaluated assuming zero yield at minimum.

The azimuthal correlation function (CF) is the distribution of the azimuthal angle (in transverse plane) between trigger and associated particles $\Delta\phi = \phi_{assoc} - \phi_{trigg}$. An example of a CF is presented in Fig. 3. One can observe a clear di-jet structure from the two peaks. The near side peak around $\Delta\phi = 0$ is formed by the particles in the same jet with the trigger. Similarly the away side peak around $\Delta\phi = \pi$ comes from the jet that, in an ideal two-to-two processes, is back-to-back with the near side jet in the transverse plane due to momentum conservation. The flat pedestal under the two jets peaks is generated from correlations that are not related with the hard interactions, i.e. the azimuthally isotropic underlying event (UE) of the proton-proton collision. Later, we will subtract this combinatorial background from the raw distributions to obtain the jet related correlations.

The relative projection of the transverse momentum of the associated particle to the direction of the trigger particles transverse momentum is called x_{E} [29],

$$x_{\mathrm{E}} = -\frac{\vec{p}_{\mathrm{Ta}} \cdot \vec{p}_{\mathrm{Tt}}}{p_{\mathrm{Tt}}^2} = -\frac{p_{\mathrm{Ta}} \cos\Delta\phi}{p_{\mathrm{Tt}}}, \tag{7}$$

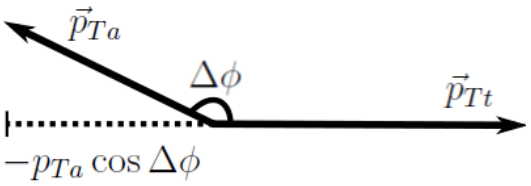

Figure 4: Illustration of a trigger (p_{Tt}) and associated (p_{Ta}) particle transverse momenta in the transverse plane.

where $p_{\mathrm{Tt}} \equiv |\vec{p}_{\mathrm{Tt}}|$ is the transverse momentum of the trigger particle, $p_{\mathrm{Ta}} \equiv |\vec{p}_{\mathrm{Ta}}|$ is the transverse momentum of the associated particle and $\Delta\phi$ is the azimuthal angle between them. A schematic picture clarifying x_{E} is shown in Fig. 4.

Another momentum fraction relevant to this study is the imbalance parameter [29]

$$x_{\mathrm{h}} = \frac{p_{\mathrm{Ta}}}{p_{\mathrm{Tt}}}, \tag{8}$$

which is particularly interesting at partonic level as it gives the momentum imbalance between the scattered partons and thus the imbalance between the near and away side jets.

2.2 CCOR Collaboration

The CCOR experiment at CERN-ISR enabled the most effective use of two-particle correlations at the time, with a p_{Tt}-range of $3 < p_{\mathrm{Tt}} < 11$ GeV and $\sqrt{s} = 62.4$ GeV for $p + p$ collisions. Especially the capacity to perform momentum analysis of charged particles over the full azimuth allowed CCOR to see clearly the jet structure of hard scattering using two-particle correlations [30].

An important part of the theoretical background for two-particle correlations of the time was the seminal paper by Feynman, Field and Fox [31]. The paper investigates correlations among particles and jets in hadronic collisions, with the assumption that jets originate from a single hard scattering of quarks from the incident hadrons.

In our case the relevant argument from [31] was that the away-side dis-

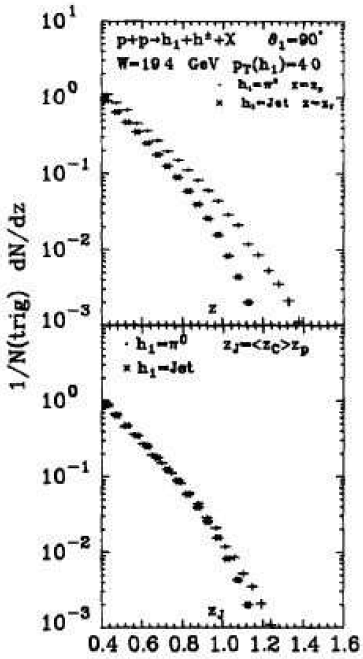

Fig. 23. Comparison of the π^0 and jet trigger away-side distribution of charged hadrons in pp collisions at $W = 19.4$ GeV, $\theta_1 = 90°$, and $p_\perp$ (trigger) = 4.0 GeV/c from the quark-quark scattering model. The upper figure shows the single-particle (π^0) trigger results plotted *versus* $z_p = -p_x(h^\pm)/p_\perp(\pi^0)$ and the jet trigger plotted *versus* $z_J = -p_x(h^\pm)/p_\perp$(jet) (see table 1). In the lower figure, we plot *both versus* z_J, where for the jet trigger $z_J = z_j$ but for the single-particle trigger $z_J = \langle z_c \rangle z_p$. The away hadrons are integrated over all rapidity Y and $|180° - \phi| \leq 45°$ and the theory is calculated using $\langle k_\perp \rangle_{h \to q} = 500$ MeV. • $h_1 = \pi^0$, × h_1 = jet.

Figure 5: Parton momentum distributions calculated in [31] exhibiting $x_{\rm E}$ scaling.

tribution should be the roughly the same when using jet triggers as when using a single-particle trigger at $p_{\rm T}$(jet)= $p_{\rm T}$(single-particle)/ $\langle z_{\rm t} \rangle$, where $z_{\rm t} = p_{\rm Tt}/\hat{p}_{\rm Tt}$. This argument involved the usual expectation that the jet transverse momentum is approximately equal to the parton momentum, i.e. $p_{\rm T,jet} \approx \hat{p}_{\rm Tt}$. Experimental data supporting this is presented in Fig. 5, where the upper panel shows both jet and π^0 triggered $x_{\rm E}$ distributions. In the lower panel the π^0-tiggered distribution has been scaled with $1/\langle z_{\rm t} \rangle$ resulting in nearly uniform distributions. Further results affirming this argument were found by various collaborations in CERN-ISR [32].

It was known that single-particle triggered jets had a trigger-bias, mean-

ing that the inclusive single particle spectrum from jet fragmentation is dominated by the trigger fragments with large $z_{\rm t}$. However, if the above argument was true, the away-side distribution should be unbiased and could thus be used to get measurements on the away-side fragmentation process, once corrected for $\langle z_{\rm t} \rangle$ and for the fact that the jets don't balance exactly (so-called $k_{\rm T}$-smearing effect). This statement also implies that the hard scattering kinematics remain fixed even if $p_{\rm Ta}$ varies as long as $p_{\rm Tt}$ is fixed.

The CCOR collaboration measured, among other things, away-side two-particle correlations. It was assumed, based on the above argument of [31], that $x_{\rm E}$ would approximate the away-side fragmentation variable $z_{\rm a}$= $p_{\rm Ta}/\hat{p}_{\rm Ta}$ in the limit of balanced back-to-back jets. Here the term balanced refers to

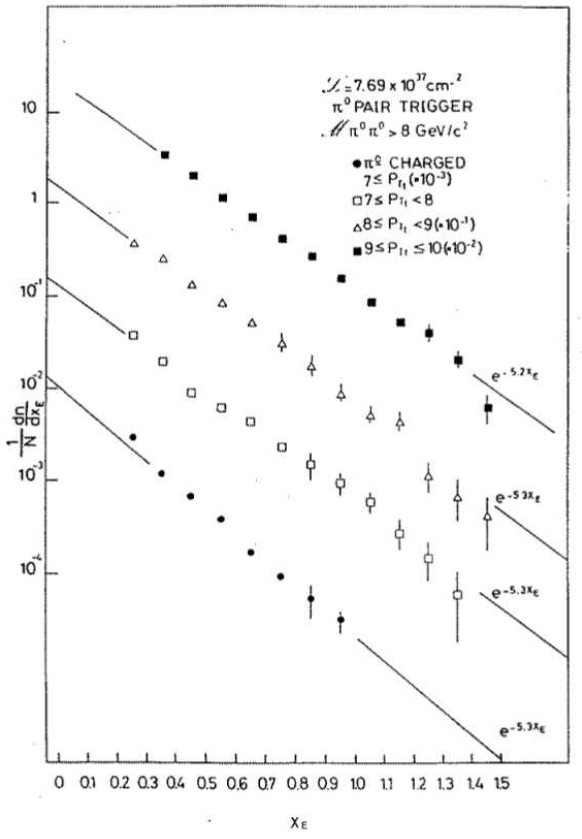

Figure 6: Measured $x_{\rm E}$ distributions from CCOR with exponential fits [33].

the ideal case where the trigger and the associated parton are back-to-back and have equal momenta. This approximation is based on the following chain of limits

$$x_{\mathrm{E}} \equiv -\frac{\vec{p}_{\mathrm{Tt}} \cdot \vec{p}_{\mathrm{Ta}}}{p_{\mathrm{Tt}}^2} \overset{\Delta\phi\to\pi}{\longrightarrow} \frac{\hat{p}_{\mathrm{Ta}} z_{\mathrm{a}}}{\hat{p}_{\mathrm{Tt}} \langle z_{\mathrm{t}} \rangle} \overset{k_{\mathrm{T}}\to 0}{\longrightarrow} \frac{z_{\mathrm{a}}}{\langle z_{\mathrm{t}} \rangle}, \tag{9}$$

where k_{T} denotes the partonic transverse momentum which is responsible for the momentum imbalance and acoplanarity of the trigger and the associated parton in the transverse plane. In this limit we can write the fragmentation function as $D(z_{\mathrm{a}}) \sim D(x_{\mathrm{E}} \langle z_{\mathrm{t}} \rangle)$.

The x_{E} distributions from CCOR gave encouraging results. They're are illustrated in Fig. 6 [33]. The CCOR Collaboration assumed the fragmentation functions to be exponential. The exponential fits followed the expected behaviour $e^{\alpha x_{\mathrm{E}} \langle z_{\mathrm{t}} \rangle}$ and seemed to scale in x_{E}. This gave reassurance that x_{E} could be used as an approximation of fragmentation function and that single-particle and jet triggers could be related simply through $\langle z_{\mathrm{t}} \rangle$.

2.3 PHENIX Collaboration

The PHENIX experiment at RHIC investigates high energy collisions of heavy ions (HI) to discover and study Quark-Gluon Plasma (QGP) which is a phase of matter which consists of asymptotically free quarks and gluons. Compelling evidence for this new phase of matter was indeed found and reported by PHENIX [34] and other RHIC experiments [35–37] in 2003.

Although the main goal of PHENIX lay on HI collisions, $p+p$ collisions were also needed as reference. To this end, PHENIX repeated many of the analyses made by the CCOR collaboration, including x_{E} analysis. However, measurements at higher energy at RHIC lead to some surprises over the expectations from ISR.

Fig. 7 presents PHENIX measurements for jet properties using non-leading particle $\pi^0 - h^{\pm}$-correlations in $p+p$ collisions at $\sqrt{s} = 200$ GeV. The non-leading particle correlations were used because PHENIX had limited azimuthal acceptance. The x_{E} distributions from these measurements are illustrated in Fig. 7 similarly to those from CCOR shown in Fig. 6. The

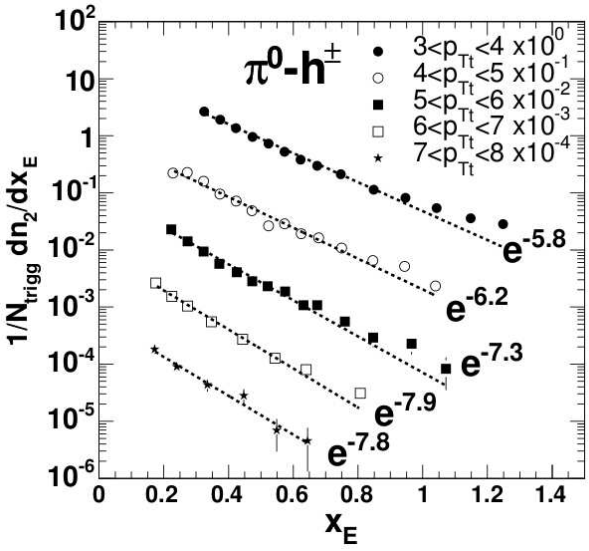

Figure 7: Measured $x_{\rm E}$ distributions with exponential fits from p+p collisions at $\sqrt{s} = 200$ GeV from PHENIX [29].

dashed lines represent the exponential fits. It is apparent that the slopes of the exponential fits seem to decrease with $p_{\rm Tt}$ and range from -5.8 to -7.8. This differs considerably from the same measurements from CCOR, where the slopes were all approximately 5.3 and independent of $p_{\rm Tt}$. In addition to this, the distributions are not quite exponential, which can be seen at high $x_{\rm E}$.

To examine this more, PHENIX studied the analytical form of the $x_{\rm E}$ distribution. According to [29], the joint probability for a fragment neutral pion with $p_{\rm Tt} = z_{\rm t}\hat{p}_{\rm Tt}$ originating from parton with $\hat{p}_{\rm Tt}$ and a charged associated particle with $p_{\rm Ta} = z_{\rm a}\hat{p}_{\rm Ta}$, originating from the other parton in the hard-scattered pair with $\hat{p}_{\rm Ta}$, is

$$\frac{d^3\sigma_\pi(\hat{p}_{\rm Ta}, z_{\rm t}, z_{\rm a})}{\hat{p}_{\rm Tt} d\hat{p}_{\rm Tt} dz_{\rm t} dz_{\rm a}} = \Sigma(\hat{p}_{\rm Tt}) D_\pi^q(z_{\rm t}) D_\pi^q(z_{\rm a}), \tag{10}$$

where

$$\Sigma(\hat{p}_{\rm Tt}) = \frac{dN_q}{d\hat{p}_{\rm Tt}} \text{ and} \tag{11}$$

$$z_{\rm a} = \frac{p_{\rm Ta}}{\hat{p}_{\rm Ta}} = \frac{p_{\rm Ta}}{\hat{x}_{\rm h}\hat{p}_{\rm Tt}} = \frac{z_{\rm t}p_{\rm Ta}}{\hat{x}_{\rm h}p_{\rm Tt}}. \tag{12}$$

A change of variables from $\hat{p}_{\rm Tt}$, $z_{\rm t}$ to $p_{\rm Tt}$, $z_{\rm t}$ and from $z_{\rm a}$ to $p_{\rm Ta}$ gives

$$\frac{d^3\sigma_\pi}{dp_{\rm Tt}dz_{\rm t}dp_{\rm Ta}} = \frac{1}{\hat{x}_{\rm h}p_{\rm Tt}}\Sigma_q(\frac{p_{\rm Tt}}{z_{\rm t}})D_\pi^q(z_{\rm t})D_\pi^q\left(\frac{z_{\rm t}p_{\rm Ta}}{\hat{x}_{\rm h}p_{\rm Tt}}\right). \tag{13}$$

Integrating this over $z_{\rm t}$ gives

$$\frac{d^2\sigma}{dp_{\rm Tt}dp_{\rm Ta}} = \frac{1}{\hat{x}_{\rm h}p_{\rm Tt}}\int_{z_{\rm t}^{min}}^{z_{\rm t}^{max}} dz_{\rm t}\Sigma_q(\frac{p_{\rm Tt}}{z_{\rm t}})D_\pi^q(z_{\rm t})D_\pi^q\left(\frac{z_{\rm t}p_{\rm Ta}}{\hat{x}_{\rm h}p_{\rm Tt}}\right), \tag{14}$$

where the integration limits for $z_{\rm t}$ are $z_{\rm t}^{min} = 2p_{\rm Tt}/\sqrt{s} = x_{\rm Tt}$ and $z_{\rm t}^{max} = \hat{x}_{\rm h}\frac{p_{\rm Tt}}{p_{\rm Ta}}$. This equation can be transformed into the $x_{\rm E}$ distribution with fixed $p_{\rm Tt}$ at the collinear limit where $p_{\rm Ta}$=$x_{\rm E}p_{\rm Tt}$, with a change of variables from $p_{\rm Ta}$ to $x_{\rm E}$. This yields

$$\frac{d^2\sigma}{dp_{\rm Tt}dx_{\rm E}} = \frac{dp_{\rm Ta}}{dx_{\rm E}} \times \frac{d^2\sigma}{dp_{\rm Tt}dp_{\rm Ta}} \approx \frac{1}{\hat{x}_{\rm h}}\int_{x_{\rm Tt}}^{\hat{x}_{\rm h}\frac{p_{\rm Tt}}{p_{\rm Ta}}} \Sigma_q(\frac{p_{\rm Tt}}{z_{\rm t}})D_\pi^q(z_{\rm t})D_\pi^q\left(\frac{z_{\rm t}p_{\rm Ta}}{\hat{x}_{\rm h}p_{\rm Tt}}\right)dz_{\rm t}. \tag{15}$$

PHENIX originally planned to extract the fragmentation function from a joint fit to the measured $x_{\rm E}$ and inclusive $p_{\rm Tt}$ distributions which had the form (Eq. 29 from [29])

$$\frac{1}{p_{\rm Tt}}\frac{d\sigma_\pi}{dp_{\rm Tt}} \approx \frac{A}{p_{\rm Tt}^n}\int_{x_{\rm Tt}}^1 dz_{\rm t}D_\pi^q(z_{\rm t})\cdot z_{\rm t}^{n-2}. \tag{16}$$

This attempt was however unsuccessful due to convergence issues. To study this issue further PHENIX calculated the $x_{\rm E}$ distributions according to Eq. (15) for quark and gluon jet fragmentation. The fragmentation functions were approximated as exponential functions $D_q(z) \approx \exp(-8.2\cdot z)$ and $D_g(z) \approx \exp(-11.4\cdot z)$, where the slopes, where obtained from LEP measurements [38, 39]. The surprising results are illustrated in Fig. 8. From it we can see that even though the fragmentation functions differ significantly the resulting $x_{\rm E}$ distributions are nearly the same. This led to the conclusion that $x_{\rm E}$ distributions from non-isolated hadrons are, in fact, not sensitive to

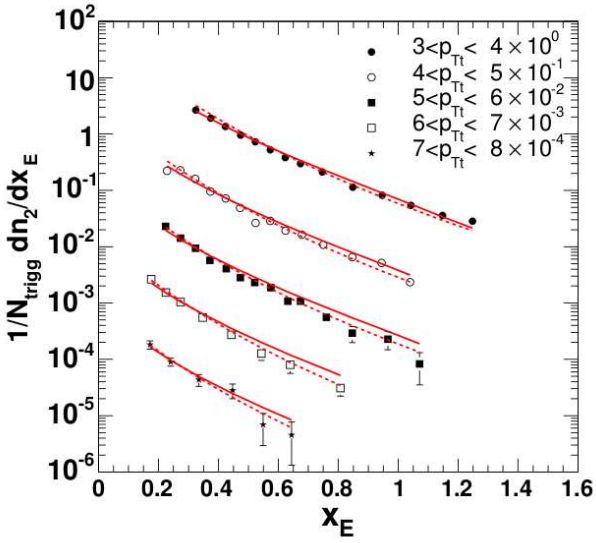

Figure 8: Measured $x_{\rm E}$ distributions with calculations according to Eq. (15) for quark (solid line) and for gluon (dashed line) $D(z) \approx \exp(-bz)$ from $p+p$ collisions at $\sqrt{s} = 200$ GeV from PHENIX [29].

the fragmentation function.

In light of this discovery PHENIX attempted to solve Eq. (14) and (16) analytically. The trigger parton spectrum was taken as a power law,

$$\Sigma_q\left(\frac{p_{\rm Tt}}{z_{\rm t}}\right) = A\left(\frac{p_{\rm Tt}}{z_{\rm t}}\right)^{-(n-1)} \tag{17}$$

and the fragmentation function as an exponential $D_\pi^q(z_{\rm t}) = B\exp(-bz_{\rm t})$, as before. With these substitutions Eq. (14) becomes

$$\frac{d^2\sigma}{dp_{\rm Tt}dp_{\rm Ta}} = \frac{B^2}{\hat{x}_{\rm h}}\frac{A}{p_{\rm Tt}^n}\int_{x_{\rm Tt}}^{\hat{x}_{\rm h}\frac{p_{\rm Tt}}{p_{\rm Ta}}} dz_{\rm t} z_{\rm t}^{n-1}\exp\left[bz_{\rm t}\left(1+\frac{p_{\rm Ta}}{\hat{x}_{\rm h}p_{\rm Tt}}\right)\right] \tag{18}$$

and Eq. (16) becomes

$$\frac{d\sigma_\pi}{dp_{\rm Tt}} = \frac{AB}{p_{\rm Tt}^{n-1}}\int_{x_{\rm Tt}}^{1} dz_{\rm t} z_{\rm t}^{n-2}\exp(-bz_{\rm t}). \tag{19}$$

These are both incomplete gamma functions (it was assumed that $\hat{x}_{\rm h}$ is con-

stant). To acquire a reasonable approximation for these integrals the upper integration limits of both integrals were taken to infinity and the lower ones to zero, thus converting them to simple gamma functions. According to the relation

$$\int_0^\infty dt\, t^\beta e^{-\alpha t} = \frac{\Gamma(\beta+1)}{\alpha^{\beta+1}} \tag{20}$$

equations (18) and (19) give

$$\frac{d^2\sigma}{dp_{\mathrm{Tt}}dp_{\mathrm{Ta}}} \approx \frac{\Gamma(n)}{b^n}\frac{B^2}{\hat{x}_{\mathrm{h}}}\frac{A}{p_{\mathrm{Tt}}^n}\frac{1}{(1+\frac{p_{\mathrm{Ta}}}{\hat{x}_{\mathrm{h}}p_{\mathrm{Tt}}})^n} \tag{21}$$

$$\frac{d\sigma_\pi}{dp_{\mathrm{Tt}}} \approx \frac{\Gamma(n-1)}{b^{n-1}}\frac{AB}{p_{\mathrm{Tt}}^{n-1}} = \frac{\Gamma(n)}{(n-1)b^{n-1}}\frac{AB}{p_{\mathrm{Tt}}^{n-1}} \tag{22}$$

where the relation $\Gamma(n) = (n-1)\Gamma(n-1)$ was used. Now the conditional probability for observing a charged associated particle with momentum p_{Ta} for neutral pion trigger particle with p_{Tt} is the ratio of the joint probability Eq. (21) to the inclusive probability (22)

$$\left.\frac{dP}{dp_{\mathrm{Ta}}}\right|_{p_{\mathrm{Tt}}} \approx \frac{B(n-1)}{bp_{\mathrm{Tt}}}\frac{1}{\hat{x}_{\mathrm{h}}}\frac{1}{(1+\frac{p_{\mathrm{Ta}}}{\hat{x}_{\mathrm{h}}p_{\mathrm{Tt}}})^n}, \tag{23}$$

which in the collinear limit $p_{\mathrm{Ta}} = x_{\mathrm{E}}p_{\mathrm{Tt}}$ finally gives an interesting and simple form for the x_{E} distribution

$$\left.\frac{dP}{dx_{\mathrm{E}}}\right|_{p_{\mathrm{Tt}}} \approx \frac{B}{b}\frac{(n-1)}{\hat{x}_{\mathrm{h}}}\frac{1}{(1+\frac{x_{\mathrm{E}}}{\hat{x}_{\mathrm{h}}})^n}. \tag{24}$$

From this form we can explicitly see that the x_{E} distribution is not very sensitive to the fragmentation function. The only dependence is the normalization constant B/b which equals the mean multiplicity of particles in the jet $\langle m\rangle$

$$\langle m\rangle = \int_0^1 D(z)dz = B\int_0^1 e^{-bz} = B/b(1-e^b) \approx B/b, \tag{25}$$

whereas the dominant term is the modified Hagedorn function $(1+x_{\mathrm{E}}/\hat{x}_{\mathrm{h}})^{-n}$.

Based on the above calculation PHENIX argued in [29] that the reason for x_{E} not being sensitive to the fragmentation function was because the integration of z_{t} integrates over both the near and away jet fragmentation function which can be seen directly in Eqs. (15) and (14) where z_{t} is present in both fragmentation functions. Another way to see this is that even with a fixed value of p_{Tt} sampling different values of p_{Ta} also changes $\langle z_{\mathrm{t}} \rangle$, which would mean that fixing p_{Tt} doesn't fix the hard scattering kinematics as previously believed.

It should be noted that even though hadron-hadron correlations now appeared to not be useful for approximating the fragmentation functions the $\gamma - h^{\pm}$ correlations should still be useful for it if the trigger is isolated. This is because if the trigger is an isolated photon it should have $\langle z_{\mathrm{t}} \rangle = 1$, as photons don't have internal structure.

ALICE Collaboration at CERN-LHC has also analysed x_{E} distributions in proton-proton collisions at $\sqrt{s} = 7$ TeV using leading particle triggered correlations and published preliminary data on the results [40, 41]. In the following, I will present the same analysis at $\sqrt{s} = 2.76$ TeV from ALICE data and discuss the results both at 2.76 TeV and 7 TeV.

3 ALICE experiment

The ALICE experiment is an international collaboration involving over 1000 members from 132 institutes and 36 countries. Its primary goal is to study the formation and properties of a new phase of matter, the quark-gluon plasma through lead-lead collisions.

3.1 ALICE detector

The ALICE detector [42] was optimized for the very high multiplicity environment created in central heavy-ion collision. For this, it was designed to feature tracking and particle identification over a large range of momenta from tens of MeV to over 100 GeV, and to be able to reconstruct huge amounts of tracks accurately with full acceptance. The ALICE detector also covers

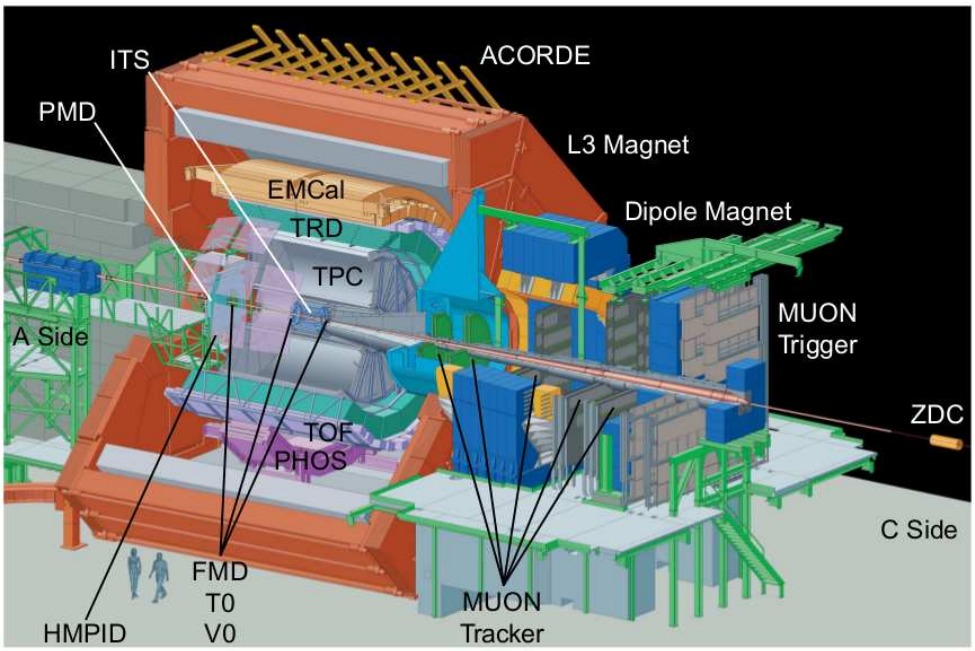

Figure 9: Illustration of the ALICE detector [43]

mainly the central region $|\eta| < 0.9$. However, it contains also some detectors in the forward region. Figure 9 shows an illustration of the ALICE detector with all of its subdetectors.

The main section of ALICE is the central barrel, which is a collection of subdetectors responsible for tracking and particle identification, enclosed in a 0.5 T magnetic field. The primary subdetectors are the Inner Tracking System (ITS), the Time-Projection Chamber (TPC), the Transition-Radiation Detector (TRD) and the Time-of-Flight detector (TOF). Of these, I will discuss the detectors relevant to this thesis: the ITS, TPC and the V0. For a detailed account of the ALICE detector see [42].

3.1.1 ITS, TPC and V0

The ITS is the innermost detector in ALICE with a radius of only 43.6 cm. Its main task is to reconstruct the primary vertex and secondary vertices of heavy quark decays and hyperons. It is also involved in particle identification

through information on energy-loss and tracking. In addition, it is capable of stand-alone tracking of low-momentum particles.

ITS consists of six layers of silicon detectors. The first two layers are called the Silicon Pixel Detector (SPD). Being closest to the interaction vertex, the SPD has to sustain a very large particle density, exceeding 50 particles per cm^2. Because of this, its readout is given in a binary form, whereas the outer layers have an analog readout. Due to its binary readout, SPD is involved only in tracking and measuring charged-particle multiplicity. Additionally, it is used to trigger events. Further details on event selection and triggering will be discussed later. The third and fourth layers, called the Silicon Drift Detector (SDD), and the two outermost layers, called the Silicon Strip Detector (SSD), are involved in both tracking and particle identification.

The TPC is a gas detector consisting of a cylindrical $90\,\mathrm{m}^3$ field cage with a length of 5 m. It's divided in two sections by a central electrode at the interaction point $z = 0$, where z is the beam direction. At both end-caps there are multi-wire proportional chambers that operate as readout planes and as anodes for the 100 kV drift (electric) field stretched across the field cage. The maximum drift time in the TPC gas is about $90\,\mu\mathrm{s}$.

The TPC is the main tracking device of the ALICE detector. It's able to track particles with in the full azimuth and at $|\eta| < 0.9$ for tracks that reach the outer radius of the cylinder. It's involved in particle identification, and in determining the momentum and production vertex of charged particles. It's able to measure tracks with p_T from 0.1 GeV up to 100 GeV and it can reconstruct and identify up to 20 000 tracks in one event.

The V0 is a small angle detector that consists of two arrays of scintillator counters at both sides of the interaction point at $z = 3.4\,\mathrm{m}$ and $z = -0.9\,\mathrm{m}$. It's primary task is triggering events, but it also participates in the measurement of luminosity in $p + p$ collisions and provides e.g. centrality and event plane measurements in the heavy ion collisions.

Not all events that occur during an experiment are useful. To select desired events, triggers are employed. The minimum-bias trigger [44] aims to trigger all inelastic interactions to impose the least possible bias. The minimum-bias trigger can be set to require a signal from either the V0 or the

SPD, or from both. Despite of the sizable extent of the triggering cabability in rapidity, the minimum bias trigger sees only a fraction of in-elastic cross section, although it is a very sizable one [45]. However, the correlation measurements are simpler in a sense that one considers per-trigger measurements, and hence, the absolute normalization to the number of in-elastic events is not needed.

3.2 Track selection

Trajectories and energies of the particles produced in collisions are stored as tracks. They are defined by five track-parameters, which give the transverse momentum and curvature of the trajectory, the scattering angle, and the distance from the interaction vertex in the beam direction and in the transverse plane. In addition to this, tracks include a covariance matrix which represents the precisions of each five track-parameters [43].

Tracks need to be reconstructed from the output of the detector. The first step is to combine signals originating from the same particles into clusters. This combining allows us to determine the exact position of the traversing particle and reduce the effects of random noise. Clusters are then combined to form tracks.

The sample of tracks acquired from the reconstruction process includes so called primary particles, as well as secondary particles. Primary particles are all particles produced in the collision, including products of strong and electromagnetic decays, as well as weak decays of charmed and beauty particles. Non-primary particles are called secondary particles which include for example feed-down products from strange weak decays, γ-conversions and products from secondary hadronic interactions with the detector material. In what follows, primary and secondary particles will be called 'primaries' and 'secondaries', respectively.

3.3 Track quality cuts

To ensure that the track quality is good and to reduce the amount of secondaries, a series of cuts are performed on the sample. These cuts can be

Accepted pseudorapidity range	$\|\eta\| < 0.8$
Maximal DCA to vertex in XY	$0.0182 \text{ cm} + 0.0350 \text{ cm } (p_{\mathrm{T}}/[\text{ GeV}/c])^{-1.01}$
Maximal DCA to vertex in Z	2 cm
Minimal number of TPC clusters	70
Maximal χ^2 per one TPC cluster	4.0
Do not accept kink daughters	
Require TPC refit	
Require ITS refit	

Table 1: Track quality cuts used in this analysis.

applied by imposing quality criteria on the properties of the track. The cuts used in the data and in my analysis are presented in Table 1.

Quality criteria can be imposed on the number of clusters used for the reconstruction of a track. The quality of the track can be controlled also with the value of χ^2 per cluster. This value gives the quality of the fit between the track and the contributing clusters.

If a charged particle decays inside the tracking volume into another charged particle with the same sign, e.g. by emitting a neutrino, it appears to change trajectory for no reason. These are called kinks. The two charged particles appear as separate tracks, but during the reconstruction the two tracks are identified as being related. The particles are flagged as the kink mother and kink daughter. Kink daughters are sometimes cut to enhance track quality.

The closest point of a tracks trajectory to the primary vertex is called the Distance of Closest Approach (DCA). As all primary particles should originate from the primary vertex, a cut on the DCA should be an effective way to remove secondaries from the sample. There two types of DCA-cuts used: an absolute and a normalized DCA-cut.

The absolute DCA-cut can be applied separately in two dimensions

$$\Delta r < d_r \quad \text{and} \quad \Delta z < d_z, \tag{26}$$

or in combination

$$\left(\frac{\Delta r}{d_r}\right)^2 + \left(\frac{\Delta z}{d_z}\right) < 1, \tag{27}$$

which results in an elliptic cut. The absolute DCA-cut is favoured if the vertex position and track parameter resolutions are imprecise.

In the normalized DCA-cut the distance to the vertex is normalized to take into account the resolutions of the track parameters and the vertex position. The normalized distance to the vertex is defined by

$$d_\sigma = \sqrt{\left(\frac{\Delta r}{\sigma_r^{DCA}}\right)^2 + \left(\frac{\Delta z}{\sigma_z^{DCA}}\right)^2}, \tag{28}$$

where σ_r^{DCA} and σ_z^{DCA} take into account the resolutions of the vertex position and track parameters. The cut is then made by choosing a number of standard deviations (N_σ) of tracks allowed, assuming they were distributed like a two-dimensional Gaussian. The cut is applied through the relation

$$N_\sigma = \sqrt{2}\,\mathrm{erf}^{-1}(1 - \exp(-d_\sigma^2/2) \tag{29}$$

where erf^{-1} is the inverse error function.

In principle, the normalized DCA-cut is superior to the absolute cut, as it uses more of the measured information. However, if the accuracy of the resolutions is imprecise, as it is e.g. in early data-taking, the absolute cut is favoured over the normalized cut.

3.4 Efficiency and contamination

The success of the cuts is measured through efficiency and contamination. Both values are evaluated through simulations. In my analysis I use tracking efficiency provided in [46]. The discussion below follows this reference.

Efficiency tells the probability that a primary particle is reconstructed and passes the employed cuts. It is defined as a ratio

$$\text{efficiency} = \frac{M(p_\mathrm{T})}{G(p_\mathrm{T})}, \tag{30}$$

where $M(p_\mathrm{T})$ is the number of reconstructed primary tracks with momentum p_T, and $G(p_\mathrm{T})$ is the number of true physical primaries. Contamination gives

the percentage of secondaries in the data set. It is defined as

$$\text{contamination} = \frac{B(p_{\mathrm{T}})}{M(p_{\mathrm{T}}) + B(p_{\mathrm{T}})}, \tag{31}$$

where $B(p_{\mathrm{T}})$ is the number of secondaries.

The aim of the cuts is to have a high efficiency and a low contamination. Selecting the cuts is thus a process of optimization. Strict cuts lead to less contamination, but at the cost of efficiency, as we also lose more primaries. Loose cuts ensure we don't lose as many primaries but at the same time we include more secondaries. The cuts employed are always fine-tuned to fit the experiment in question. Some experiments require higher efficiency and some lower contamination.

Efficiency and contimination are based on a Monte Carlo study where PYTHIA events [47] are generated and particles ran through a simulation of a detector response in ALICE. The final outcome of this full simulation is presented in Fig. 10.

To minimize the effects caused by lost primaries and contamination by secondaries the data is corrected for efficiency. The efficiency correction is

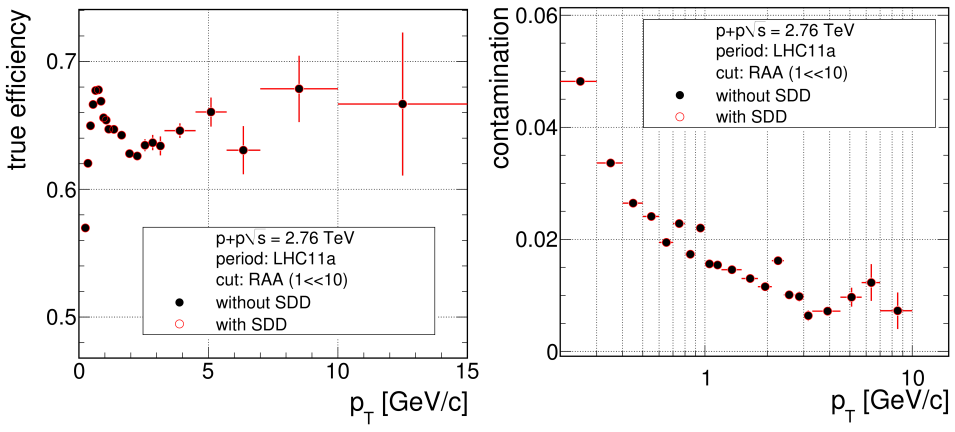

Figure 10: Efficiency and contamination of reconstructed charged tracks selected with cuts listed in Tab. 1.

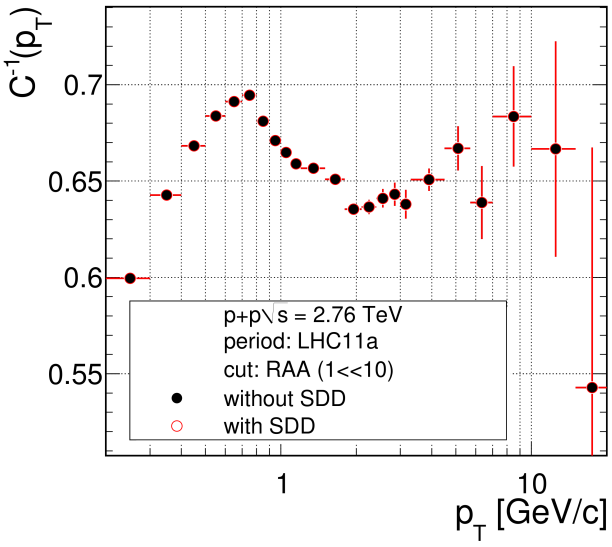

Figure 11: Inverse of the efficiency correction of reconstructed charged tracks selected with cuts listed in Tab. 1.

defined as

$$C^{-1}(p_{\mathrm{T}}) = \frac{M(p_{\mathrm{T}}) + B(p_{\mathrm{T}})}{G(p_{\mathrm{T}})}. \tag{32}$$

The final efficiency correction in this analysis is presented in Fig. 11

4 Analysis

In my analysis, I used ROOT [48,49], an object-oriented data-analysis framework based on C++. ROOT was developed for large scale data analysis and simulation of particle physics. It includes a library of useful objects to analyse and store data, and to illustrate this data.

My analysis was done on data from $p+p$ collisions at $\sqrt{s} = 2.76$ TeV measured by ALICE. The data was stored as histograms representing various distributions and organized in p_{Tt}-bins. The p_{Tt}-range was from 4 GeV to 30 GeV and the bin borders were the following: $\{4, 5, 6, 7, 8, 10, 14, 20, 30\}$. The two last bins ($14 < p_{\mathrm{Tt}} < 20$ GeV and $20 < p_{\mathrm{Tt}} < 30$ GeV) were cut on the account of lack of statistics. The associated p_{T} range was 1 GeV $< p_{\mathrm{Ta}} <$

p_{Tt}.

The x_{E} distributions had earlier been analysed in ALICE [50], and at $\sqrt{s} = 7$ TeV proton-proton collisions preliminary results have been reached [40, 41]. Here I aim to finalize the results at 2.76 TeV collisions and compare the results with the 7 TeV data and earlier measurements by CCOR and PHENIX.

4.1 Underlying event background

The largest task in the analysis was the extraction of the underlying event background. This background includes contributions from pairs where one or both of the particles do not originate from the hard scattering, called uncorrelated pairs.

A raw associated x_{E} distribution, that includes correlated and uncorrelated pairs, is made by calculating x_{E} with Eq. (7) between the selected trigger particle and the particles on the away-side in the same event. This means the raw distribution comprises of

$$\begin{aligned}\left(\frac{dN}{dx_{\mathrm{E}}}\right)_{raw} &= \left(\frac{dN}{dx_{\mathrm{E}}}\right)_{correlated} + \left(\frac{dN}{dx_{\mathrm{E}}}\right)_{uncorrelated} \\ &= \left(\frac{dN}{dx_{\mathrm{E}}}\right)_{correlated} + \left(\frac{dN}{dx_{\mathrm{E}}}\right)_{jet-BG} + \left(\frac{dN}{dx_{\mathrm{E}}}\right)_{BG-BG}, \end{aligned} \tag{33}$$

where jet-BG is the case where the trigger or associated particle is a background particle while the other one is a jet-particle, and BG-BG is the case where both are background particles. In leading particle correlations the BG-BG component is small compared to the jet-BG and jet-jet component because when one chooses a high-p_{T} trigger particle it is likely that it's from a jet.

4.1.1 Analytic formula of the uncorrelated x_{E} background

To get a better understanding of the uncorrelated background of the away side x_{E} distribution, I examined it analytically [51]. In principle, the shape of

the background can be calculated assuming that the background is isotropic in $\Delta\phi$ and that the behaviour of the background as a function of p_{Ta} is known. The assumption, $dN/d\Delta\phi = \text{const.}$, is well justified as underlying events shouldn't have any preferred direction. With these assumptions, I could write

$$\left.\frac{d^2N}{dp_{\mathrm{Ta}}d\Delta\phi}\right|_{p_{\mathrm{Tt}}} = B_{p_{\mathrm{Tt}}}(p_{\mathrm{Ta}}). \tag{34}$$

Let's now examine the background with a fixed p_{Tt}. The shape of the background is described by the form

$$\begin{aligned}\frac{dN_{bg}}{dx_{\mathrm{E}}} &= \int_{\pi/2}^{3\pi/2} d(\Delta\phi) \int_{p_{\mathrm{Ta}}^{min}}^{p_{\mathrm{Tt}}} dp_{\mathrm{Ta}} \left.\frac{d^2N}{dp_{\mathrm{Ta}}d\Delta\phi}\right|_{p_{\mathrm{Tt}}} \delta(x_{\mathrm{E}} + \frac{p_{\mathrm{Ta}}}{p_{\mathrm{Tt}}}\cos\Delta\phi) \\ &= \int_{\pi/2}^{3\pi/2} d(\Delta\phi) \int_{p_{\mathrm{Ta}}^{min}}^{p_{\mathrm{Tt}}} dp_{\mathrm{Ta}} B_{p_{\mathrm{Tt}}}(p_{\mathrm{Ta}}) \delta(x_{\mathrm{E}} + \frac{p_{\mathrm{Ta}}}{p_{\mathrm{Tt}}}\cos\Delta\phi),\end{aligned} \tag{35}$$

where the delta-function selects only pairs with given x_{E}. The integration limits of $\Delta\phi$ cover the away side. The lower limit of the p_{Ta} range is p_{Ta}^{min} and the upper limit is the momentum of the trigger particle, as I'm considering leading particle correlations. To integrate over p_{Ta} I wrote the delta function as

$$\delta(x_{\mathrm{E}}+\frac{p_{\mathrm{Ta}}}{p_{\mathrm{Tt}}}\cos\Delta\phi) = \left|\frac{p_{\mathrm{Tt}}}{\cos\Delta\phi}\right| \delta\left(\frac{p_{\mathrm{Tt}}}{\cos\Delta\phi}x_{\mathrm{E}} + p_{\mathrm{Ta}}\right) = -\frac{p_{\mathrm{Tt}}}{\cos\Delta\phi}\delta\left(\frac{p_{\mathrm{Tt}}}{\cos\Delta\phi}x_{\mathrm{E}} + p_{\mathrm{Ta}}\right), \tag{36}$$

where the absolute values gives a minus sign because I'm examining the away side, $\Delta\phi \in [\frac{\pi}{2}, \frac{3\pi}{2}]$. Now the integration over p_{Ta} gives

$$\frac{dN_{bg}}{dx_{\mathrm{E}}} = -\int_{\pi/2}^{3\pi/2} d(\Delta\phi) \int_{p_{\mathrm{Ta}}^{min}}^{p_{\mathrm{Tt}}} dp_{\mathrm{Ta}} B(p_{\mathrm{Ta}}) \frac{p_{\mathrm{Tt}}}{\cos\Delta\phi} \delta\left(\frac{p_{\mathrm{Tt}}}{\cos\Delta\phi}x_{\mathrm{E}} + p_{\mathrm{Ta}}\right) \tag{37}$$

$$= -2\int_{\phi_{min}}^{\phi_{max}} d(\Delta\phi) B\left(-\frac{p_{\mathrm{Tt}}}{\cos\Delta\phi}x_{\mathrm{E}}\right) \frac{p_{\mathrm{Tt}}}{\cos\Delta\phi}, \tag{38}$$

where the integration limits of $\Delta\phi$ change because the delta-function gives non-zero results only when $p_{\mathrm{Ta}}^{min} < -\frac{p_{\mathrm{Tt}}}{\cos\Delta\phi}x_{\mathrm{E}} < p_{\mathrm{Tt}}$. This constrains the integration limits for $\Delta\phi$ to $\phi_{min} = \arccos(-x_{\mathrm{E}})$ and $\phi_{max} = \arccos\left(-\frac{p_{\mathrm{Tt}}}{p_{\mathrm{Ta}}^{min}}x_{\mathrm{E}}\right)$.

However as $\arccos(x)$ is defined only within a range $x \in [-1,1]$, but $p_{\mathrm{Ta}}^{min} < p_{\mathrm{Tt}}$ and $x_{\mathrm{E}} \in [0,1]$, $\frac{p_{\mathrm{Tt}}}{p_{\mathrm{Ta}}^{min}} x_{\mathrm{E}}$ can have values smaller than -1. Hence the maximum angle is

$$\phi_{max} = \begin{cases} \arccos(-\frac{p_{\mathrm{Tt}}}{p_{\mathrm{Ta}}^{min}} x_{\mathrm{E}}) & \frac{p_{\mathrm{Tt}}}{p_{\mathrm{Ta}}^{min}} x_{\mathrm{E}} \leq 1 \\ \pi & \frac{p_{\mathrm{Tt}}}{p_{\mathrm{Ta}}^{min}} x_{\mathrm{E}} > 1 \end{cases} . \tag{39}$$

Above I considered the uncorrelated background at fixed p_{Tt}. In reality, the distributions are examined in bins with finite width. So instead of a fixed single value, the p_{T} of the trigger follows some $dN/dp_{\mathrm{Tt}}(p_{\mathrm{Tt}})$-distribution in a given p_{Tt}-bin $p_{\mathrm{Tt}}^{min} < p_{\mathrm{Tt}} < p_{\mathrm{Tt}}^{max}$. To take this into account I had to integrate the background distribution over the p_{Tt}-bin and weight it with the p_{Tt} distribution which lead to

$$\frac{dN_{bg}}{dx_{\mathrm{E}}} = -\int_{p_{\mathrm{Tt}}^{min}}^{p_{\mathrm{Tt}}^{max}} dp_{\mathrm{Tt}} \int_{\phi_{min}}^{\phi_{max}} d(\Delta\phi) \frac{dN}{dp_{\mathrm{Tt}}} B\left(\frac{-p_{\mathrm{Tt}}}{\cos\Delta\phi} x_{\mathrm{E}}\right) \frac{p_{\mathrm{Tt}}}{\cos\Delta\phi}. \tag{40}$$

Integration of Eq.(40) cannot be done analytically, but I could still learn something from this formula. Looking at Eq. (40) it can be seen that as long as $\frac{p_{\mathrm{Tt}}}{p_{\mathrm{Ta}}^{min}} x_{\mathrm{E}} < 1$, or $x_{\mathrm{E}} < \frac{p_{\mathrm{Ta}}^{min}}{p_{\mathrm{Tt}}}$ the x_{E}-background is affected by the applied phase space cut $p_{\mathrm{Ta}} > p_{\mathrm{Ta}}^{min}$. The higher the value of p_{Tt} and smaller the cut, the smaller the x_{E}-range affected by the cut.

Instead of evaluating Eq. (40) numerically, I used a Monte Carlo implementation of the background determination. A clear benefit from this approach is that I could generate histograms directly for the background that were then very simple to subtract from the raw yield. In the following sections, I will present the generation of the background and how it is normalized. I will also present the systematic uncertainties of the measurement.

4.2 Background x_{E} distribution form

To calculate values of x_{E}, I needed sources to sample values of p_{Tt}, p_{Ta} and $\Delta\phi$ from. I assumed that uncorrelated particles don't have a preferred direction,

so the $\Delta\phi$-source was a uniform distribution at $\pi/2 < \Delta\phi < 3\pi/2$. For the sources of p_{Tt} and p_{Ta} I used fits of the p_{Tt} distribution and underlying event p_{Ta} distribution, respectively. I will discuss the exact nature of these fits momentarily.

To get the form of the x_{E} background in a single p_{Tt}-bin, I calculated ten million values of x_{E}. In my loop within a fixed trigger bin I first sampled p_{Tt} and p_{Ta} by taking a random value from their respective sources and checked that the sampled value of p_{Tt} was greater than the value of p_{Ta}. If this was not true I discarded these values and sampled a new pair . When a satisfactory p_{Tt}-p_{Ta} pair was sampled the loop then continued to sample a value of $\Delta\phi$ by taking a random value from a uniform distribution with range $[0.5, 1.5]$ and multiplied this with π. I then used these values to calculate x_{E} according to Eq. (7) and finally inserted this value into a histogram. After ten million iterations of the above loop, I normalized the now formed background distribution to unity. I repeated this procedure for each p_{Tt}-bin.

4.2.1 Trigger particle p_{T} distribution

The source for p_{Tt} was a fit of the trigger particle p_{T}-distribution. These distributions were compiled by identifying the leading particle of each event and then inserting it into a p_{Tt}-histogram in the corresponding p_{Tt}-bin. It was required that the trigger particle has a minimum transverse momentum of 4.0 GeV's.

p_{Tt}-bin	n	Stat. error	χ^2/NDF
$4-5$	5.09	0.05	0.90
$5-6$	5.20	0.09	0.59
$6-7$	5.4	0.2	1.13
$7-8$	5.9	0.3	1.98
$8-10$	5.7	0.2	0.82
$10-14$	5.4	0.2	1.29

Table 2: Magnitudes of the power-law exponent n extracted from fits of p_{Tt} distributions and the corresponding χ^2/NDF values.

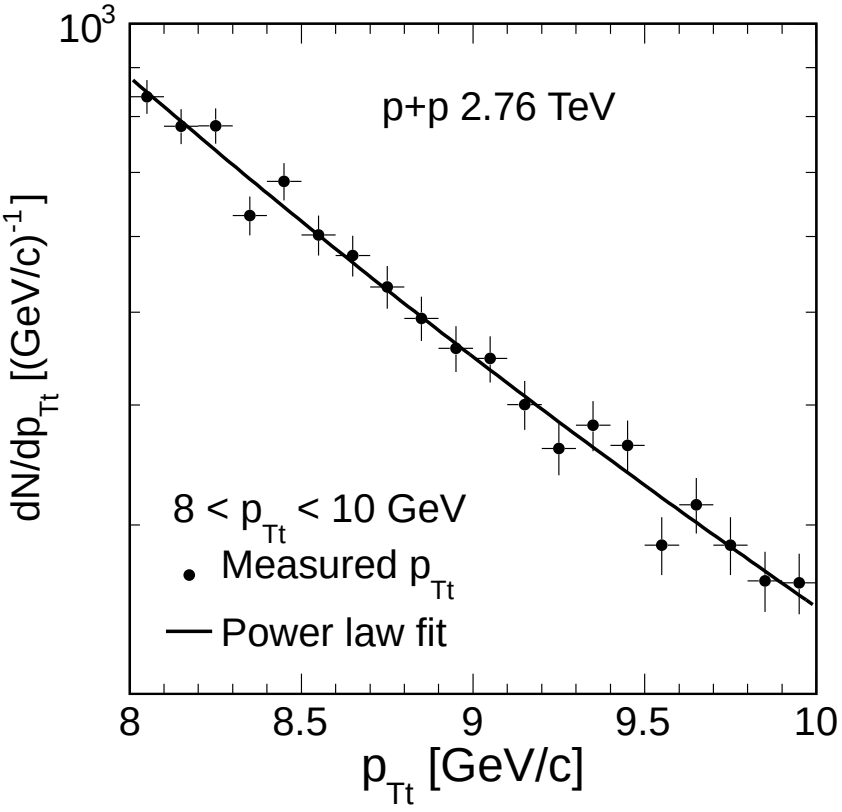

Figure 12: Trigger p_{T} distribution with a power law fit at $8 < p_{\mathrm{Tt}} < 10$ GeV from $p+p$ collisions at $\sqrt{s} = 2.76$ TeV

The p_{Tt} distributions are expected to follow a power law function

$$f(p_{\mathrm{Tt}}) \propto p_{\mathrm{Tt}}^{-n}. \tag{41}$$

In Fig. 12, I present an example of these fits in p_{Tt} bin $8 < p_{\mathrm{Tt}} < 10$ GeV. All p_{Tt} distributions with power law fits can be found in Appendix A. The exponents n of each fit with errors and χ^2/NDF values can be found in Tab. 2. As one can see from Fig. 12 the power law follows the p_{Tt} distribution nicely throughout and in all the distributions. The last bin $10 < p_{\mathrm{Tt}} < 14$ GeV begins to show some signs of running out of statistics but the fluctuations are still reasonable. The χ^2/NDF values also show that the fits were quite

successful. The fits give a slightly rising trend for n, but the variation is small.

4.2.2 Underlying event p_{Ta} distribution

The source for p_{Ta} was a fit of the underlying event p_{Ta} distribution. In compiling this distribution it was assumed that particles moving perpendicular to the trigger particle were most likely to be uncorrelated particles originating from underlying events. This means that the underlying event p_{Ta} spectrum was estimated by the p_{T} spectrum of particles close to the minima of the correlation function. I've illustrated this range in Fig. 13. The difficulty was how to choose this range. A small range has less statistics but if the range is increased the contamination by correlated particles also increases. In my analysis, the underlying p_{Ta} distributions were compiled by selecting particles from $\Delta\phi$ ranges of $0.325 < \Delta\phi < 0.475$ rad/π and $1.525 < \Delta\phi < 1.675$ rad/π.

In Fig. 14b, I show an example of the underlying event p_{Ta} distribution at p_{Tt}-bin $8 < p_{\mathrm{Tt}} < 10$ GeV. From these one can see that the used data set didn't have an abundance of statistics. Only the first two distributions have statistics from the whole available p_{Ta}-range. These two exhibit a rapidly falling tail at the range corresponding to the p_{Tt}-bin borders. These tails

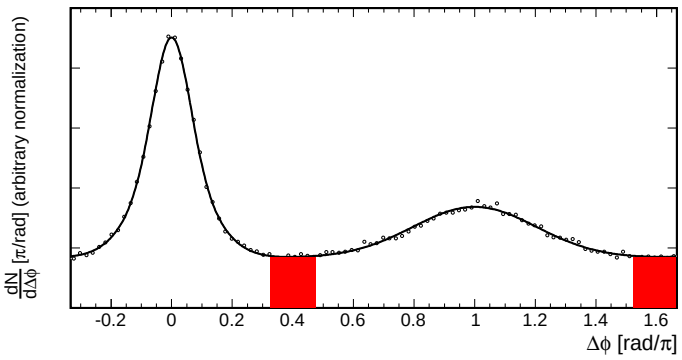

Figure 13: Example of an azimuthal correlation function illustrating the $\Delta\phi$ ranges which were used to estimate the p_{Ta} distribution of underlying events

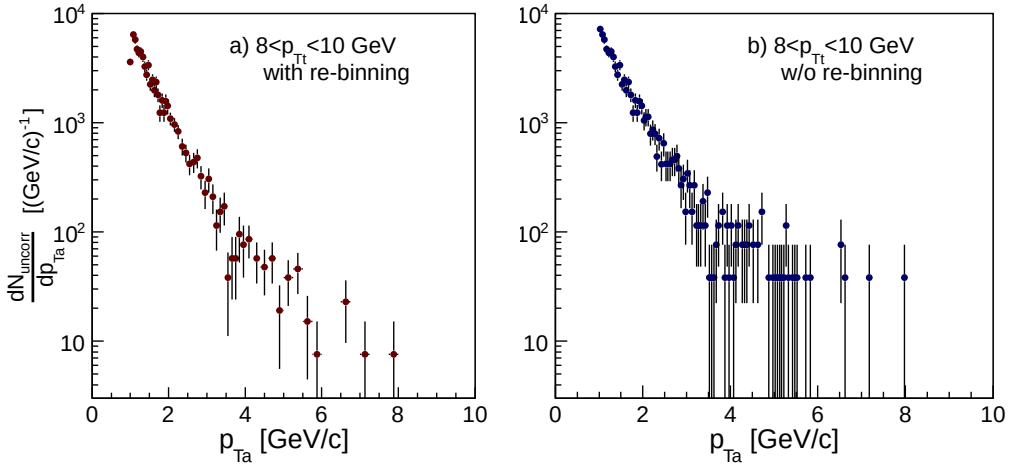

Figure 14: Underlying event p_{Ta} distribution at $8 < p_{\mathrm{Tt}} < 10$ GeV a) with re-binning and b) without re-binning

are an effect of the requirement $p_{\mathrm{Ta}} < p_{\mathrm{Tt}}$. Fortunately the contributions from these tails to the final x_{E} background distribution are so small that the limited knowledge of the tails does not lead into substantial uncertainties in the final results.

To further combat the lack of statistics, I attempted to enhance the p_{Ta} distributions by re-binning them. The original distributions had equally wide bins. My general approach was to widen the bins as p_{Ta} grows to make the high-p_{Ta} tail more useful.

The outline of the bin borders can be found in Tab. 3 (left). I then attempted to further fine-tune the borders by combining and dividing bins. I evaluated the quality of the choice of borders visually and by examining the χ^2/NDF values of the fit I performed on the p_{Ta} distribution. Details of these fits will be discussed later. Fine-tuning was difficult as usually when one distribution was enhanced the others became worse.

Fig. 14 shows the positive effects of the re-binning at $8 < p_{\mathrm{Tt}} < 10$ GeV. It is clear that the original distribution on the right seems to become unreliable at $p_{\mathrm{Ta}} > 4$ GeV. On the left side, it can be seen that the re-binning has successfully stretched the useful p_{Ta}-range almost up to 8 GeV.

Now that I had better binned p_{Ta} distributions, I could start fitting them with an appropriate function. I used the Kaplan function for the fit. It's of the form

$$G(p_{\mathrm{Ta}}) = A_0 \left(1 + \frac{(p_{\mathrm{Ta}} - a_1)^2}{a_2}\right)^{-\beta}. \tag{42}$$

When fitting with a function of four parameters it's important to remember that one set of initial parameters can give a different fit than another set. Due to this I experimented with the initial parameters of the fit and finally settled on the following initial parameters: $\beta = 3.0$, $a_1 = 0$, $a_2 = 2.0$. The initial value for parameter A_0 was determined by the maximum of each p_{Ta} distribution.

The range of my fit to the p_{Ta} distributions was from 1 GeV to the lower border of the corresponding p_{Tt}-bin. This leaves the range influenced by the requirement $p_{\mathrm{Ta}} < p_{\mathrm{Tt}}$ out of the fit. The range also excludes the first p_{Ta} bin, because the bin border of the histogram didn't match the cut on soft particles. Fortunately, despite having quite small statistics, each distribution had some contributions in the range of the fit, excluding the last bin whose statistics run out at $p_{\mathrm{Ta}} \approx 8$ GeV. This gives reassurance that the fits describe the distributions correctly.

In Fig. 15, I show an example of the Kaplan fit to the p_{Ta} distributions at $8 < p_{\mathrm{Tt}} < 10$ GeV. Rest of the fits and p_{Ta} distributions can be found in Appendix A. In these figures I've plotted the fitted function all the way to the upper border of the p_{Tt}-bin. From these it can be seen that the fit follows

p_{Ta}-range	Bin width [GeV]	p_{Tt}-bin	χ^2	NDF	χ^2/NDF
$0-2$	0.05	$4-5$	45.0	56	0.80
$2-4$	0.1	$5-6$	41.7	40	1.04
$4-5$	0.2	$6-7$	44.3	44	1.01
$5-8$	0.25	$7-8$	38.2	46	0.83
$8-10$	0.5	$8-10$	44.1	47	0.94
$10-16$	1.0	$10-14$	43.2	47	0.92

Table 3: Left: Outline of bin widths of the underlying event p_{T} distribution after re-binning. Right: χ^2 values of the Kaplan fits of underlying event p_{Ta} spectra.

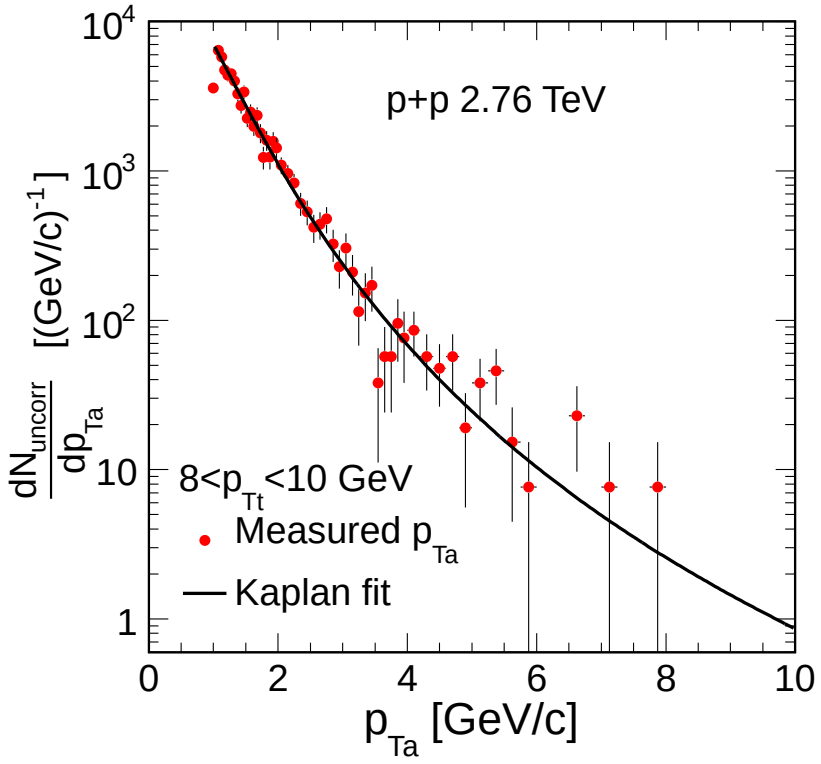

Figure 15: Fit of the Kaplan function to the underlying event p_{Ta} distribution at $8 < p_{\mathrm{Tt}} < 10$ GeV at $\sqrt{s} = 2.76$ TeV

the distribution well with, of course, the exception of the tails in the first two p_{Tt}-bins. Based on χ^2/NDF presented in Table 3 (right), the Kaplan function fitted the data very well in all p_{Tt} bins.

4.3 Normalization

For the normalization, I needed to figure out the number of uncorrelated pairs. For this I assumed that the pairs where the associated particle is uncorrelated with the trigger in azimuth, form also the background in x_{E}-space. This means the number of uncorrelated pairs of the away side of the correlation function and x_{E} are equivalent. As the uncorrelated particles should be distributed isotropically in azimuth the question was how to estimate the

number of pairs which form the underlying event pedestal i.e. the constant part below the correlation function.

The approach I used was to fit the correlation function with a sum of two functions, parametrizing the near ($P_N(\Delta\phi)$) and away side ($P_A(\Delta\phi)$) peaks, and a constant U which is the background amplitude, representing the underlying event pedestal

$$G(\Delta\phi) = P_N(\Delta\phi) + P_A(\Delta\phi) + U \tag{43}$$

The number of uncorrelated pairs would then be given by the area under the away side peak given by the integral

$$N_{bg} = \int_{\pi/2}^{3\pi/2} d(\Delta\phi)\, U = \pi U. \tag{44}$$

In this case $\Delta\phi$ was measured in units of rad/π, so the number of uncorrelated pairs was in fact $N_{bg} = U$.

4.3.1 Fits of the correlation functions

The original CFs had a really tight binning and hence I aimed to reduce statistical fluctuations by re-binning. Unlike with the p_{Ta} distributions I didn't define the borders of the bins explicitly, but combined existing bins. I re-binned all the CFs by combining two bins into one. Even after the first re-binning the first p_{Tt}-bin correlation function exhibited some heavy statistical fluctuation near its minima, which dropped the underlying event pedestal significantly. To decrease this fluctuation I combined three bins into one in the first p_{Tt}-bin. This cleaned the data near the minima sufficiently.

The functions P_N and P_A describing the two peaks are not known from

theory. I used a sum of two gaussians to parametrize each peak

$$P_N(\Delta\phi) = A_1 \exp\left[\frac{1}{2}\left(\frac{\Delta\phi - \mu_N}{\sigma_1}\right)^2\right] + A_2 \exp\left[\frac{1}{2}\left(\frac{\Delta\phi - \mu_N}{\sigma_2}\right)^2\right]$$
$$P_A(\Delta\phi) = A_3 \exp\left[\frac{1}{2}\left(\frac{\Delta\phi - \mu_A}{\sigma_3}\right)^2\right] + A_4 \exp\left[\frac{1}{2}\left(\frac{\Delta\phi - \mu_N}{\sigma_4}\right)^2\right]. \quad (45)$$

The gaussians were centered around the same mean value: $\mu_N = 0$ rad for the near side and $\mu_A = \pi$ rad for the away side. The idea behind this sum is that the other gaussian is narrow and it fits the top of the peak and the other is wider and fits the bottom of the peak.

I estimated the initial values of parameters μ_i $(i = 1, 2, 3, 4)$ according to the widths of the peaks near the top and bottom. The initial values of A_i, I estimated by the amplitudes of the peaks. I calculated these amplitude estimates by subtracting the estimate of the background from the bin content of the CF at $\Delta\phi = 0$ rad and $\Delta\phi = \pi$ rad for the near and away side peaks, respectively. I acquired the initial value for the background by calculating the average bin content of the CF at interval $0.3\pi < \Delta\phi < 0.5\pi$ rad.

I've present the result of the fit at p_{Tt} bin $8 < p_{\mathrm{Tt}} < 10$ GeV in Fig. 16. Results for the other p_{Tt} bins can be found in Appendix A. Fig. 16 also shows the background amplitude and its statistical error. From these it can be seen that especially at high p_{Tt} there is a significant amount of statistical fluctuations. Overall the used parametrization seems to describe the data well. A small anomaly can be seen in the tip of the away side peak at $6 < p_{\mathrm{Tt}} < 7$ GeV. There the transition between the wide and narrow peak isn't as smooth as with the others. This however shouldn't influence the background level significantly.

I present the χ^2/NDF values of the fit of each p_{Tt}-bin in Tab. 4. I've also presented the values and errors of the background level U and of each p_{Tt}-bin. The χ^2 statistics support the claim that the fits were successful. The first bin has a slightly higher value, but this was due to the looser binning discussed earlier. The wider bins also resulted in a smaller statistical error compared to the other fits as can be seen by the relative errors $\delta U/U$.

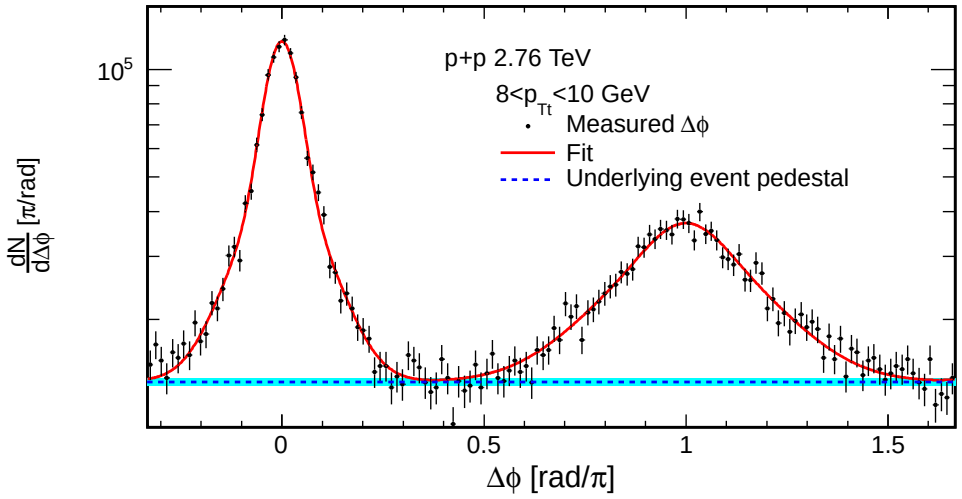

Figure 16: Fit of the azimuthal correlation function at $8 < p_{\mathrm{Tt}} < 10$ GeV and $\sqrt{s} = 2.76$ TeV with function according to Eq. (43) and (45). The blue dashed line represents the underlying event pedestal and the light blue band its statistical error.

p_{Tt}-bin	U ($\times 10^3$)	Stat.error δU ($\times 10^3$)	$\delta U/U$	χ^2/NDF
$4-5$	250.4	1.5	0.006	1.54
$5-6$	88.9	1.1	0.012	1.17
$6-7$	36.8	0.5	0.014	1.19
$7-8$	17.1	0.4	0.022	1.04
$8-10$	13.4	0.3	0.026	0.93
$10-14$	7.1	0.2	0.026	1.16

Table 4: Values of the background amplitude U with their errors and the χ^2/NDF values extracted from the fits of the azimuthal correlation functions of each p_{Tt} bin.

Based on Fig. 16 and the CF's in Appendix A the background levels set near the average minima of the data and of the fit. The acquired background levels seem realistic. The relative errors are also small.

After the acquiring the background levels U, I scaled the previously computed background forms with them to get the normalized background distributions.

4.4 Measured, signal and background x_{E}

In Fig. 17 I present the measured away side x_{E} distribution and the Monte Carlo -generated background distribution at $8 < p_{\mathrm{Tt}} < 10$ GeV without acceptance correction. The rest of these distribution can be found in Appendix A.

The background shows a peak at low x_{E}. This is caused by the requirement $p_{\mathrm{Ta}} > p_{\mathrm{Ta}}^{min} = 1$ GeV, which affects the upper integration limit ϕ_{max} in Eq. (40). The peak marks the point where the cut stops affecting the background i.e. when $x_{\mathrm{E}}\, p_{\mathrm{Tt}}/p_{\mathrm{Ta}}^{min} = 1$ and $\phi_{max} = \arccos(-x_{\mathrm{E}} p_{\mathrm{Tt}}/p_{\mathrm{Ta}}^{min})$ turns to π. The slight downward bending is caused by the lower integration limit $\phi_{min} = \arccos(-x_{\mathrm{E}})$, as when x_{E} goes approaches 1 the lower limit ϕ_{min} ap-

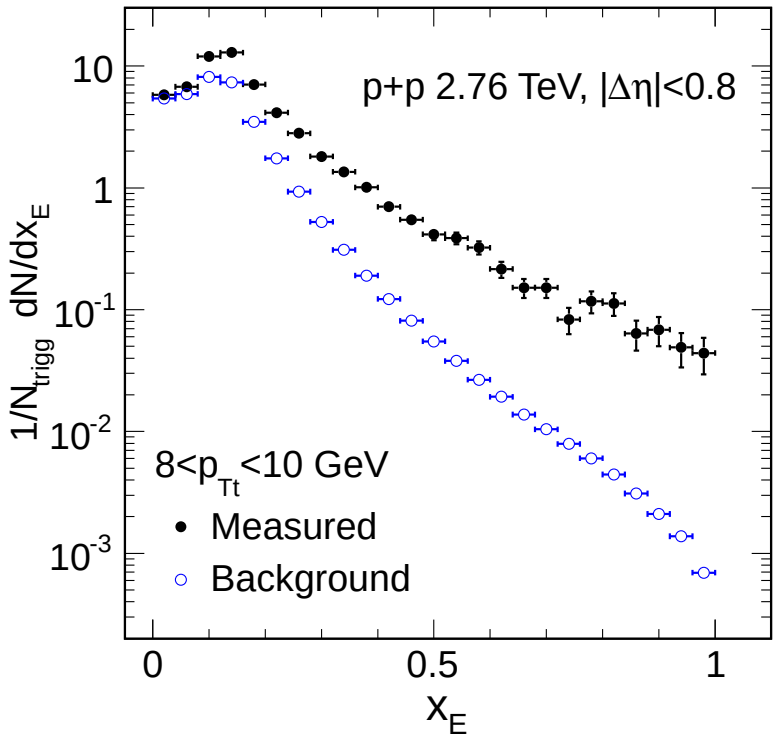

Figure 17: Measured away side x_{E} distribution and the corresponding Monte Carlo -generated background distribution at $8 < p_{\mathrm{Tt}} < 10$ GeV without acceptance correction.

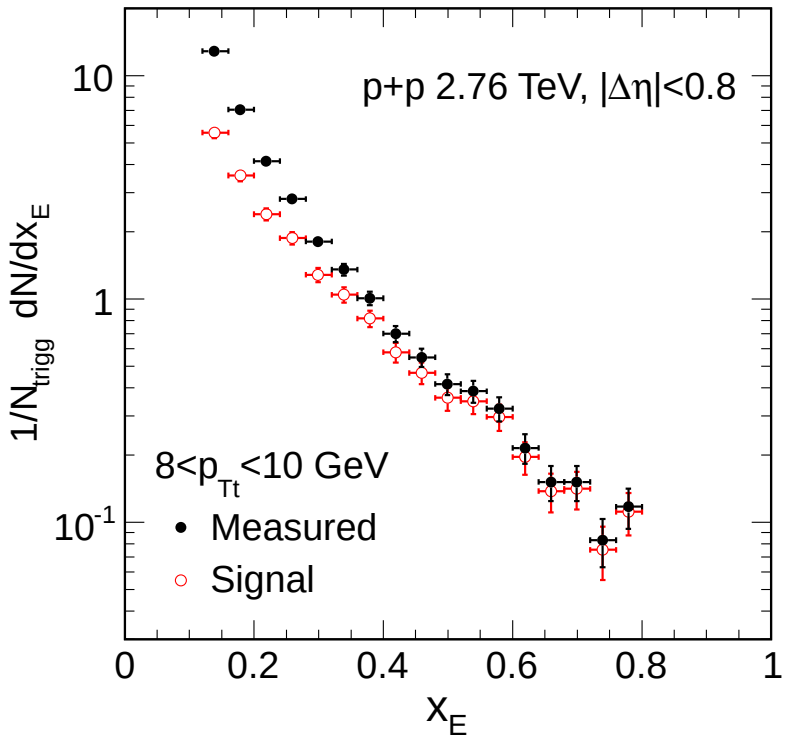

Figure 18: Signal away side x_{E} distribution and measured x_{E} distribution at $8 < p_{\mathrm{Tt}} < 10$ GeV without acceptance correction.

proaches π rapidly which results in the integration range approaching zero $\phi_{max} - \phi_{min} \to 0$.

Comparing the measured x_{E} and the background shows that the background contributions to the measured distribution are most significant at low x_{E}. This was to be expected as pairs with high x_{E} are more likely to originate from the hard scattering. Also as p_{Tt} increases the background contributions seem to become less significant, which was also expected since underlying events are less significant in high trigger bins.

The signal x_{E} distribution I acquired by subtracting the normalized background from the measured x_{E}. In Fig. 18, I show the measured away side x_{E} distribution and the signal x_{E} distribution at $8 < p_{\mathrm{Tt}} < 10$ GeV without acceptance correction. The rest of these distribution can be found in Appendix

A. I cut the points below $x_{\mathrm{E}} = p_{\mathrm{Ta}}^{min}/p_{\mathrm{Tt}} = 1/p_{\mathrm{Tt}}$ to eliminate the contributions affected by the lower cut on p_{Ta}. I also cut the tail to discard some of the contributions where $p_{\mathrm{Ta}} \in (p_{\mathrm{Tt}}^{min}, p_{\mathrm{Tt}}^{max})$. With $\cos(\Delta\phi) = -1$, the lowest point that can be affected by the p_{Tt} bin borders is when $p_{\mathrm{Ta}} = p_{\mathrm{Tt}}^{min}$ and $p_{\mathrm{Tt}} = p_{\mathrm{Tt}}^{max}$, where p_{Tt}^{max} (p_{Tt}^{min}) is the upper (lower) limit of the p_{Tt}. Based on this I cut the points above $x_{\mathrm{E}} = p_{\mathrm{Tt}}^{min}/p_{\mathrm{Tt}}^{max}$.

These figures reinforce the previous observations that the background is most significant at low x_{E} and p_{Tt}. In the first two p_{Tt} bins the measured and signal distributions are clearly distinct throughout x_{E}. As p_{Tt} grows, the two distributions start to converge. However, even at the highest p_{Tt} bins at low x_{E} the difference between the signal and measured x_{E} is significant. This causes the shape of the x_{E} distribution to become less steep when the background is removed.

4.5 Systematic errors

During my analysis of the x_{E} distributions, I encountered several sources of systematic error. These errors arise from the fact that in each stage I had several equally valid options that yielded different results. To account for the systematic error that comes from these choices I calculated the signal x_{E} distributions using these alternatives. In the following I will describe the systematic errors that were considered.

4.5.1 Systematic error sources

The underlying event p_{Ta} distribution $dN_{\mathrm{UE}}/dp_{\mathrm{Ta}}$ was compiled by choosing associated tracks near the minima of the correlation function. These regions are the least affected by the tracks from the hard scattering, but they're still not completely free of these tracks. The amount of contamination from hard scattered tracks depends on the chosen $\Delta\phi$ range. To study the effects of this choice I compiled $dN_{\mathrm{UE}}/dp_{\mathrm{Ta}}$ from $\Delta\phi$-range that was half of the original, $\Delta\phi \in (0.3625, 0.4375) \oplus (1.5623, 1.6375)\mathrm{rad}/\pi$. I've shown the p_{Ta} distributions from both $\Delta\phi$ ranges in Fig. 19. From it is can be seen that the shape of the distribution doesn't change significantly, whereas the amount of

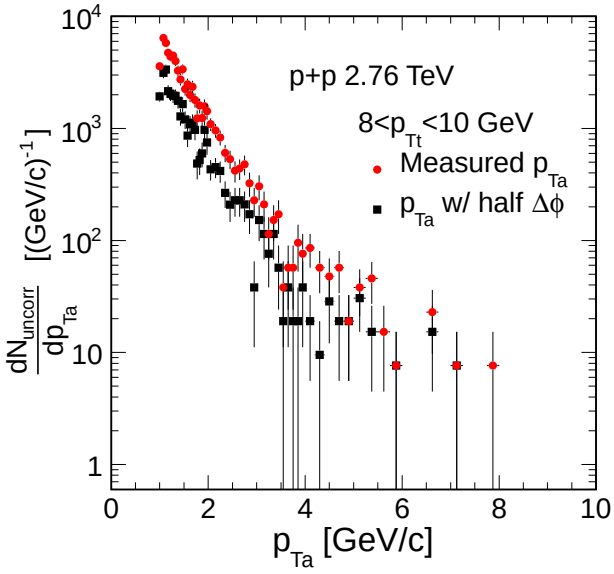

Figure 19: Underlying event p_{Ta} distributions compiled from $\Delta\phi$range $\Delta\phi \in (0.325, 0.475) \oplus (1.525, 1.675)$ rad/π (red dot) and $\Delta\phi \in (0.3625, 0.4375) \oplus (1.5623, 1.6375)$ rad/π (black square) at $8 < p_{\mathrm{Tt}} < 10$ GeV.

statistics drops as expected.

In calculating the shape of the x_{E} background, I used the Kaplan function to fit the underlying event p_{Ta} distribution. However, the correct parametrization of this distribution is yet unknown. Indeed several other functions can be used for the fit. To assess the sensitivity to this I tested an extreme case where I sampled p_{Ta} directly from the measured histogram. The same applied to p_{Tt}. The power law function is considered to be a reliable fit for the trigger p_{T} distribution. Nevertheless, I tested the sensitivity of this fit again by sampling p_{Tt} from the measured p_{Tt} histogram.

The absolute normalization depends on the function used to describe the peaks of the $dN/d\Delta\phi$ distribution. The correct parametrization of the peaks is unknown so I tested how the normalization changes when the peaks are parametrized by a different function. I used the familiar Kaplan function

$$k(x) = A(1 + ax^2)^{-n} \tag{46}$$

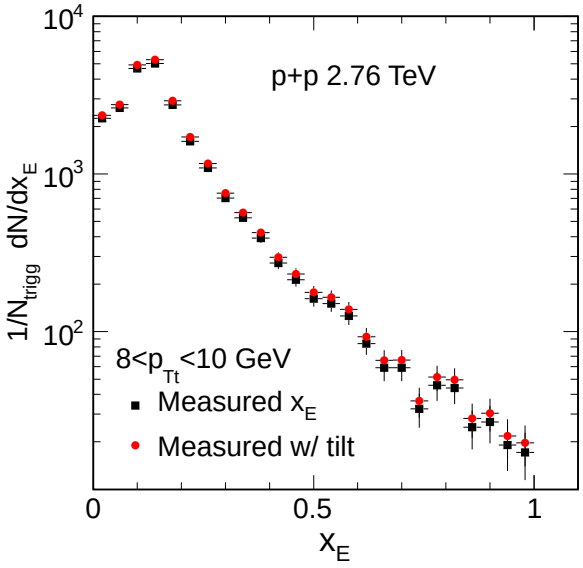

Figure 20: Measured x_{E} distributions that has been scaled with $(0.959 - 0.08959x_{\mathrm{E}})^{-1}$ (red dot) and the original (black square) at $8 < p_{\mathrm{Tt}} < 10$ GeV.

for this, as Kaplan functions can develop stronger tails than the Gaussian function. This makes it possible for the background level to drop lower. In addition to this, I also examined the extreme case where the background level was determined assuming zero yield at minimum (ZYAM). I did this by taking the minimum of a fourth order polynomial that was fit to $dN/d\Delta\phi$ in the range $\Delta\phi \in (0.24, 0.65)\mathrm{rad}/\pi$.

Corrections on reconstruction efficiency and contamination are calculated using event generators. In my analysis these corrections were calculated using PYTHIA. However one event generator can give different results than the other. Here I studied the difference in x_{E} in the case that the efficiency calculation would be based on PHOJET [52] instead of PYTHIA.

It has also been found [46, 50], that in the Monte Carlo data the ratio between simulated x_{E} distributions obtained from final efficiency-corrected data and directly determined input data is not flat but slightly tilted. This indicates that the efficiency correction might not correct for detector effects perfectly. Here I assess this ratio as a possible source of a systematic error. In

the $\sqrt{s} = 2.76$ TeV data the x_{E} tilt could be parametrized by a linear function $0.959 - 0.08959x_{\mathrm{E}}$ and the correlation function was found to be decreased by a constant of 0.95. To study the effects of these I calculated the signal x_{E} scaling the measured x_{E} with $(0.959 - 0.08959x_{\mathrm{E}})^{-1}$ and the correlation function by 1/0.95. To show how much the tilting affects the measured x_{E}, I've presented the original and tilted x_{E} distributions at $8 < p_{\mathrm{Tt}} < 10$ GeV in Fig. 20. It shows that the distribution becomes less steep, as expected from the scaling function. The change is clearly noticeable but not dramatic.

4.5.2 Signal x_{E} distribution

After I had calculated the signal x_{E} distributions for each systematic error set, I calculated the difference between them and the signal x_{E} from reference data. I then summed these differences to get the final systematic errors. Regarding absolute normalization, there was a possibility that both Kaplan and ZYAM cases had the same sign of deviation from reference. If this was the case, I considered only the error from the Kaplan case and discarded the ZYAM error.

In my analysis I made some fits to the signal x_{E} distribution. Naturally the systematic errors transfer into the parameters obtained from the fits. I calculated the systematics error to these by obtaining the values of the relevant parameters in each of the cases described above and subtracted these values from the reference values, as before.

5 Results

In Fig. 21 I present all the signal away side x_{E} distributions with systematic errors. I have truncated the distributions as in Fig. 18 and normalized by negative powers of four for clarity. From Fig. 21 it is apparent, that at the higher p_{Tt} bins the distributions start to suffer from lack of statistics when $x_{\mathrm{E}} > 0.5$. Especially with triggers ranging from 6.0 GeV to 14.0 GeV, the distributions fluctuate significantly.

The distributions appear to be nearly exponential, but at low x_{E} the dis-

tributions seems to be steeper than at high x_{E} with the exception of the first bin. This behaviour can be seen most clearly at triggers ranging from 6.0 GeV to 14 GeV. These distributions thus show similar behaviour as documented by PHENIX in Fig. 7.

To get a better understanding of the contribution of each systematic error source to the final errors, I calculated the relative differences between the signal x_{E} distributions from the reference data and the systematic error sets. In Fig. 22, I present the differences at $8 < p_{\mathrm{Tt}} < 10$ GeV. The rest of the relative differences are shown in Appendix A.

The most notable contributions are given by the tilted set. One can see that in most cases it's contributions are, at its lowest, greater than the other contributions at their highest, except the Kaplan. It also has a clear linear form whose slope seems to remain roughly the same regardless of p_{Tt}.

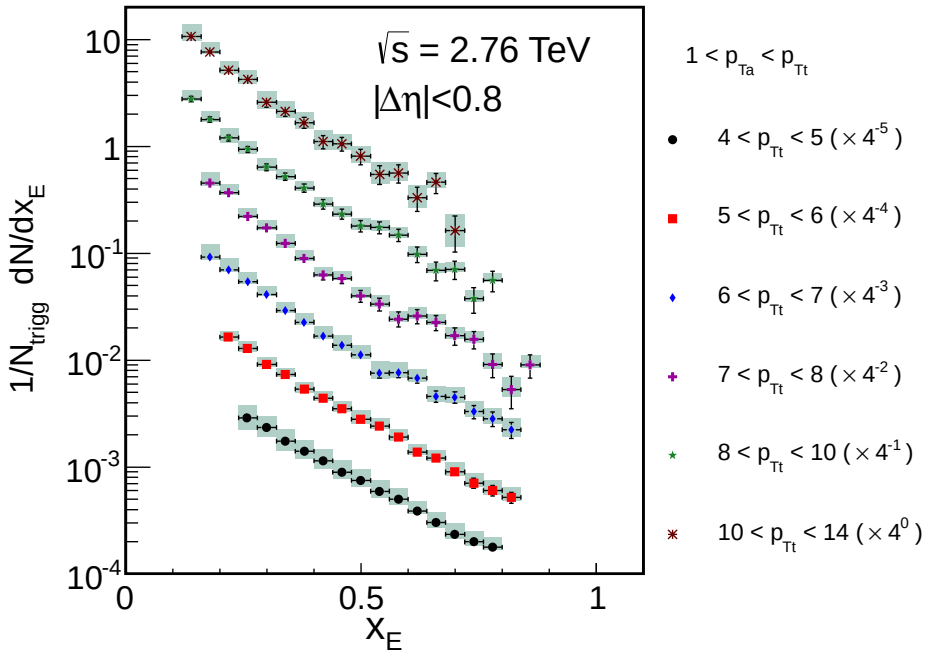

Figure 21: Signal away side x_{E} distributions at $\sqrt{s} = 2.76$ TeV in each p_{Tt} bin. The distributions have been scaled with negative powers of four. Systematic errors are shown as light grey squares.

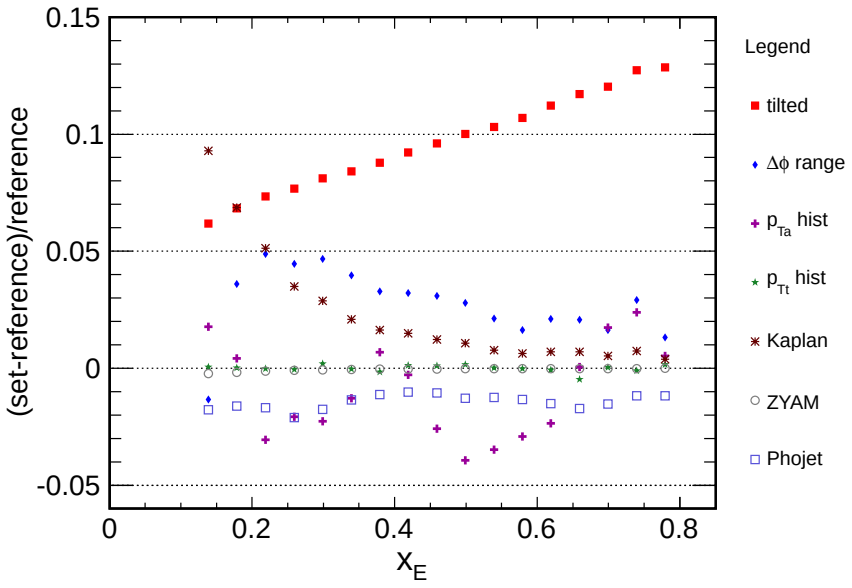

Figure 22: The relative differences of the signal x_{E} distributions between the reference data and each source of systematic error at $8 < p_{\mathrm{Tt}} < 10$ GeV.

This undoubtedly comes from the fact that in the tilted set we modified the measured x_{E} distribution with a linear function.

The sets with a modified absolute normalization (Kaplan and ZYAM) seem to have similar shapes, with the exception of the bins between $7 < p_{\mathrm{Tt}} < 10$ GeV. Both sets have strong differences at low x_{E} that quickly fade out. With the ZYAM set this effect is weaker, which reflects the fact that the Gaussian fit of the correlation function gives results very near to the ZYAM method. Based on the Kaplan set results, the choice of function used to parametrize the correlation peaks is not a trivial one.

As expected the use of the p_{Tt} histogram instead of the power law fit didn't create much deviation from the reference. The use of p_{Ta} histogram caused more differences that grow as p_{Tt} grows, undoubtedly due to decrease of statistics at high p_{Tt}.

The PHOJET set also didn't exhibit overtly high deviations. Except for the first p_{Tt} bin the difference is roughly constant throughout x_{E} and p_{Tt}.

The $\Delta\phi$ range set, where the underlying event p_{Ta} distribution was com-

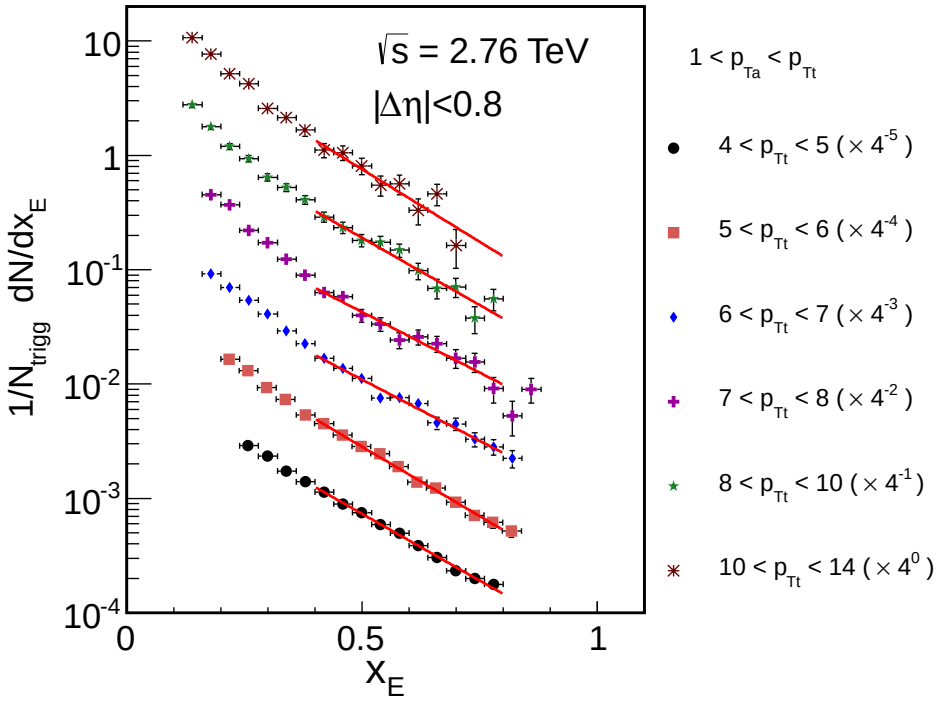

Figure 23: Signal away side x_{E} distributions at $\sqrt{s} = 2.76$ TeV in each p_{Tt} bin with exponential fits. The distributions have been scaled with negative powers of four.

piled from a smaller $\Delta\phi$ range, exhibited the most erratic behaviour. At $10 < p_{\mathrm{Tt}} < 14$ GeV we can see that the differences drop dramatically. This is likely due to the lack of statistics in the p_{Ta} distribution.

The final systematic errors seem to be of reasonable size. They also seem to be mostly inclined upward, which is because the outstanding differences, e.g. Kaplan and tilted sets, were mostly positive.

5.1 High-x_{E} exponential fit

From the signal distributions in Fig. 21, it appeared that they might exhibit uniform slopes at high x_{E}. To study this closer I fit the signal distribution with an exponential function $dN/dx_{\mathrm{E}} \propto \exp(-\alpha\, x_{\mathrm{E}})$ in the region $0.4 <$

$x_{\mathrm{E}} < 0.8$. I present the results of the fits in Fig. 23. The χ^2/NDF values and the slopes of the fit with errors can be found in Tab. 5. From Fig. 23, it is apparent that generally the fit follows the data well. The good χ^2/NDF values also indicate that the exponential function describes the tail well.

Already from Fig. 23 it can be seen that the slopes of the fits are close to one another. The values of the slopes in Tab. 5, support this observation. The two distributions between $6 < p_{\mathrm{Tt}} < 8$ GeV are noticeably less steep than the others. If the fit range was slightly bigger these slopes would probably grow closer to the others.

In Fig. 24 I show the relative differences of the exponential fit slope parameters α. As expected the tilted set shows a regular difference throughout p_{Tt}. Recall that tilting makes the slope of the x_{E} distribution less steep. The effect of this is seen directly here.

Using the p_{Tt} histogram shows again almost no difference whereas the p_{Ta} case shows significant differences at $p_{\mathrm{Tt}} > 6$ GeV. The difference is also always below 0. This is because the p_{Ta} histograms had poor statistics at high p_{Ta}, resulting in that low values of p_{Ta} were more likely to have been sampled, which made the slope less steep.

The Kaplan set shows again rather strong differences. They seem to follow the behaviour exhibited in the relative differences of x_{E}. The steeply falling differences, e.g. in Fig. 22, translates to a steeper slope. The ZYAM case also behaves accordingly. When the x_{E} difference increases the slopes

p_{Tt}-bin	Slope α	Stat.error $\delta\alpha$	χ^2/NDF
$4-5$	5.38	0.14	0.56
$5-6$	5.59	0.21	0.32
$6-7$	4.93	0.30	0.73
$7-8$	4.88	0.43	0.64
$8-10$	5.42	0.43	0.87
$10-14$	5.85	0.76	1.04

Table 5: Values of the negative exponential slope parameters with their errors and the χ^2/NDF values extracted from the fits of the signal x_{E} distributions of each p_{Tt} bin.

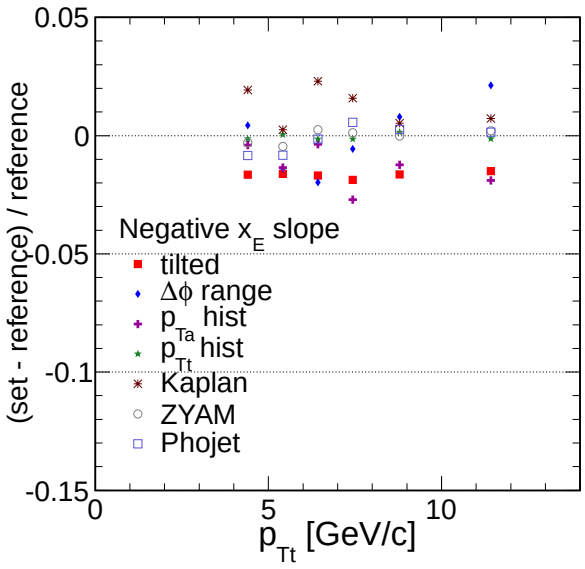

Figure 24: The relative differences of exponential fit slope parameter α between the reference data and each source of systematic error.

are less steep ($4 < p_{\mathrm{Tt}} < 6$ GeV), and when decreasing they're steeper ($6 < p_{\mathrm{Tt}} < 14$ GeV).

The PHOJET and reduced $\Delta\phi$ range sets also behave according to the x_{E} difference as with the Kaplan and ZYAM sets. The PHOJET sets differences are not as strong as the $\Delta\phi$ range sets, and the PHOJET set is less randomly distributed.

5.1.1 Slopes of the exponential fit

The negative slope parameters α from the exponential fits as a function of p_{Tt} are shown in Fig. 25 (left). With the current statistics, the errors are fairly sizeable. Also systematic errors would reduce with significantly more statistics, since many of them result from various fits into data that suffered from limited amount of statistics.

I am unable to say anything conclusive about the behaviour of the slopes α as a function of p_{Tt}, based on Fig. 25. The data can be interpreted to exhibit either a rising trend or to being flat within the errors.

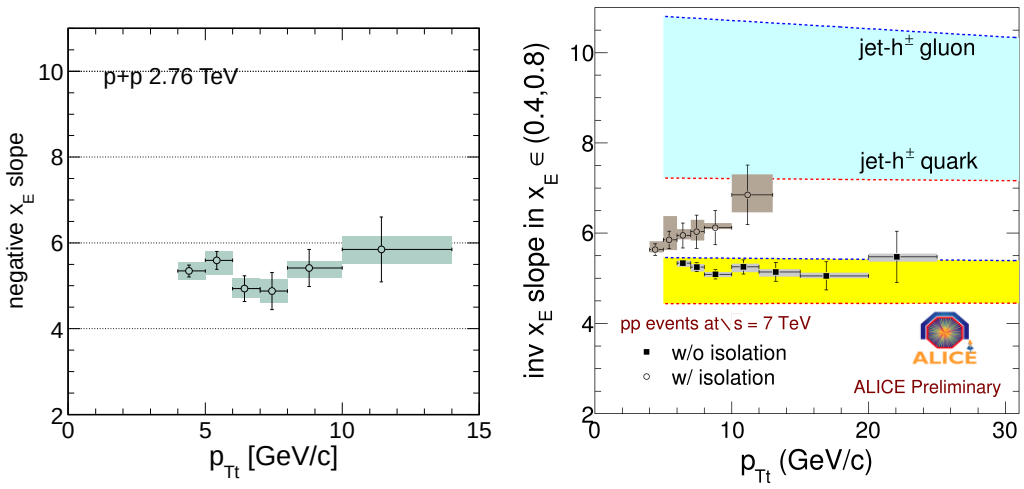

Figure 25: Left: negative slopes extracted from exponential fits to the signal x_{E} distributions as a function of p_{Tt} from $p+p$-collisions at $\sqrt{s} = 2.76$ TeV. Right: negative slopes extracted from dN/dx_{E} with a non-isolated (solid) and isolated (hollow) trigger $\sqrt{s} = 7$ TeV data [40]. The grey areas denote systematic errors. All fits were done in the range $x_{\mathrm{E}} \in (0.4, 0.8)$

The ALICE collaboration has done similar research with $\sqrt{s} = 7$ TeV data using a non-isolated and an isolated leading particle as a trigger [40]. This was done to test the idea that the tail of the x_{E} distribution would be sensitive to the mean fraction of energy carried by the trigger $\langle z_{\mathrm{t}} \rangle$. Evidence supporting this claim was indeed found.

In Fig. 25 (right), I show the preliminary results for negative x_{E} slopes by the ALICE Collaboration. The coloured belts are simple fragmentation model predictions for x_{E} slope that were calculated using the KKP parametrization for fragmentation functions [17]. The two belts in Fig. 25 are based on the following Monte Carlo simulation on simplified kinematics: first a back-to-back pair of partons is generated from a power law distribution, where the power is taken from asymptotic behaviour of the inclusive spectrum. This simulates ideal two-to-two kinematics with $k_{\mathrm{T}} = 0$. In the upper bands the trigger side is not fragmented, i.e. $\langle z_{\mathrm{t}} \rangle = 1$, corresponding to an ideal direct photon trigger. In the away side random values from gluon (quark) fragmentation function are generated and then x_{E} is filled into

histograms according to the trigger. Finally the slope is determined in the region $0.4 < x_{\mathrm{E}} < 0.8$ just like in the data which gives the upper (lower) limit for gluon (quark) FF. Lower bands represent analysis for di-hadron correlations, i.e. both back-to-back partons are fragmented and the resulting larger momentum is chosen as a trigger.

First from Fig. 25 it can be seen that the x_{E} slopes without isolation cuts seem to be constant as a function of p_{Tt}. They are also situated within the yellow belt meaning their $\langle z_{\mathrm{t}} \rangle \approx 0.5$, which further supports the result by PHENIX that the slopes of the x_{E} distribution are not sensitive to the fragmentation functions. However, this simple Monte Carlo model seems to very well catch the main features of the di-hadron data.

The isolated particles were chosen by examining the charged hadron activity inside a cone with radius $R = 0.4$ rad, $R = \sqrt{\Delta\phi^2 + \Delta\eta^2}$. It was required that within this cone the activity of tracks with $p_{\mathrm{T}} > 0.5$ GeV should stay under 10% of the particles p_{T}. The slopes with isolated triggers seem to behave differently than in the non-isolated case. They appear to exhibit a rising trend with increasing p_{Tt}. At about $2 < p_{\mathrm{Tt}} < 4$ GeV the slopes are very near the yellow belt and at $p_{\mathrm{Tt}} > 10$ GeV they are near the blue belt. This shows that in the isolated case increasing p_{Tt} also increases $\langle z_{\mathrm{t}} \rangle$. Unfortunately, as isolated leading particles are quite rare, sufficient statistics went only as far as 13 GeV. It appears plausible that increasing p_{Tt} further would result in the trigger fraction to reach $\langle z_{\mathrm{t}} \rangle = 1$.

The results shown in Fig. 25 (right) are comparable to my results (left). It appears that the slopes from the $\sqrt{s} = 2.76$ TeV data are on the upper border of the yellow belt. The difference to the $\sqrt{s} = 7$ TeV slopes could be explained by the smaller total energy $\sqrt{s}$ of the collisions.

5.2 The imbalance parameter $\langle \hat{x}_{\mathrm{h}} \rangle$

As stated previously the mean imbalance parameter in the partonic level $\langle \hat{x}_{\mathrm{h}} \rangle$ can be obtained from a fit to the x_{E} distribution with Eq. (24).

$$H(x_{\mathrm{E}}) = m(n-1)\frac{1}{\langle \hat{x}_{\mathrm{h}} \rangle}\left(1 - \frac{x_{\mathrm{E}}}{\langle \hat{x}_{\mathrm{h}} \rangle}\right)^{-n} \tag{47}$$

Parameter n was a fixed parameter that originated from the exponential slope from the trigger parton spectrum. However, based on the parent-child relationship the slope of the inclusive spectrum of charged tracks $1/(2\pi p_{\mathrm{T}})dN/dp_{\mathrm{T}}$ should be the same. The spectrum was fit in the range $p_{\mathrm{T}} \in (5, 15)$ GeV and the resulting slope was $n = 6.38$ [53]. The x_{E} distributions were fit in full range.

I present the modified Hagedorn fits to the x_{E} distributions in Fig. 26. The acquired values of $\langle \hat{x}_{\mathrm{h}} \rangle$ and χ^2 statistics I present in Tab. 6. The fits seem to follow the the distributions excellently in the lowest three p_{Tt} bins. With the highest three p_{Tt} bins, the lack of statistics starts to show in the distributions, but the fit still describes the data within the statistical uncertainties. The χ^2 statistics were also very small with χ^2/NDF staying below 1.3 in all p_{Tt} bins.

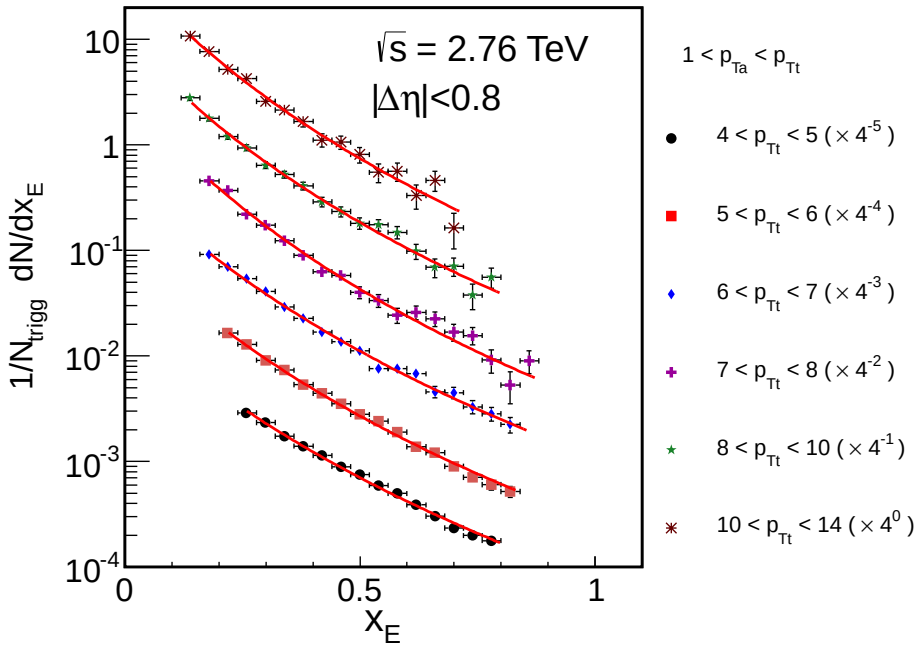

Figure 26: Signal away side x_{E} distributions at $\sqrt{s} = 2.76$ TeV in each p_{Tt} bin with fit by the modified Hagedorn function Eq. (47). The distributions have been scaled with negative powers of four.

p_{Tt}-bin	$\langle \hat{x}_{\mathrm{h}} \rangle$	Stat.error $\delta \hat{x}_{\mathrm{h}}$	χ^2/NDF
$4-5$	0.62	0.02	1.29
$5-6$	0.57	0.02	0.78
$6-7$	0.57	0.02	0.63
$7-8$	0.48	0.02	1.19
$8-10$	0.52	0.02	0.84
$10-14$	0.51	0.03	0.74

Table 6: Values of $\langle \hat{x}_{\mathrm{h}} \rangle$ with their errors and the χ^2/NDF values extracted from the modified Hagedorn function fits of the signal x_{E} distributions of each p_{Tt} bin.

I calculated the systematic errors for $\langle \hat{x}_{\mathrm{h}} \rangle$ as described in section 4.5.2. The Hagedorn fit had one extra source of systematic error, which was the slope n of the inclusive spectrum of charged tracks. This slope depends on the p_{T} range of the fit done on the spectrum dN/dp_{T}. To assess this effect I fit the dN/dp_{T} spectrum also in the ranges $8 < p_{\mathrm{T}} < 25$ GeV and $4 < p_{\mathrm{T}} < 10$ GeV which gave the exponents $n_1 = 6.41$ and $n_2 = 6.32$, respectively [53]. I then acquired the $\langle \hat{x}_{\mathrm{h}} \rangle$ using these exponents as before.

The relative differences of the $\langle \hat{x}_{\mathrm{h}} \rangle$ I present in Fig. 27 seem to be near those of the exponential slope. The strongest difference is with the Kaplan set, which exhibits noticeably bigger differences than the other sets.

The PHOJET set shows only a slight constant deviation from the reference. Using the p_{Tt} histogram caused also only a slight difference that seems to diminish with p_{Tt}. The p_{Ta} case and the tilted set show very similar behaviour as with the exponential slopes, except the deviation of the tilted set is of the opposite sign. The last point of the reduced $\Delta\phi$ range set shows again the lack of statistics that resulted from using a smaller range. Otherwise the $\Delta\phi$ range set behaves as erratic as before.

Changing the power of the inclusive charged hadron spectrum seems to affect $\langle \hat{x}_{\mathrm{h}} \rangle$ as a constant. It appears that even a slight change in the power causes noticeable differences in $\langle \hat{x}_{\mathrm{h}} \rangle$. The differences in the powers were $\Delta n_1 = 0.03$ and $\Delta n_2 = 0.06$ and they caused almost 1% and 2% changes in $\langle \hat{x}_{\mathrm{h}} \rangle$ respectively. In my case the difference was small but in general it is

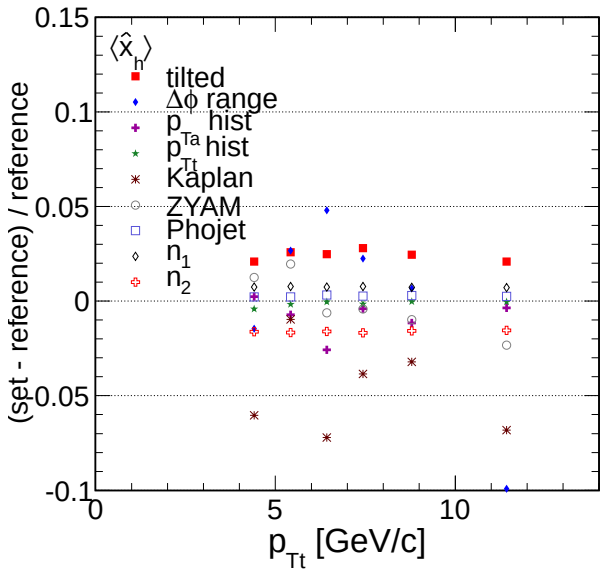

Figure 27: The relative differences of the imbalance parameter $\langle \hat{x}_{\mathrm{h}} \rangle$ from the modified Hagedorn fit between the reference data and each source of systematic error. Labels $n_1 = 6.40896$ and $n_2 = 6.31638$ refer to the power of the inclusive charged hadron spectrum.

possible for the differences of the power to go at least as high as 0.27 [50], which can lead to significant systematic errors.

Looking at the values of $\langle \hat{x}_{\mathrm{h}} \rangle$ in Tab. 6, they seem to decrease with p_{Tt}. In Fig. 28 I show $\langle \hat{x}_{\mathrm{h}} \rangle$ as a function of p_{Tt}. It shows that the decrease with p_{Tt} is not very strong. It should be pointed out that while the statistical errors are small, the systematic errors are, as with the x_{E} slopes, quite large. With this few points to consider and large systematic errors it's difficult to say anything conclusive on the behaviour of $\langle \hat{x}_{\mathrm{h}} \rangle$ other than that it decreases with p_{Tt}, at least up to a point.

The most relevant observation that can be made from Fig. 28 is that it is always below 1. This is strong evidence for trigger-bias. It shows that already the trigger parton is always harder than the associated parton. So trigger bias is present already at the partonic level.

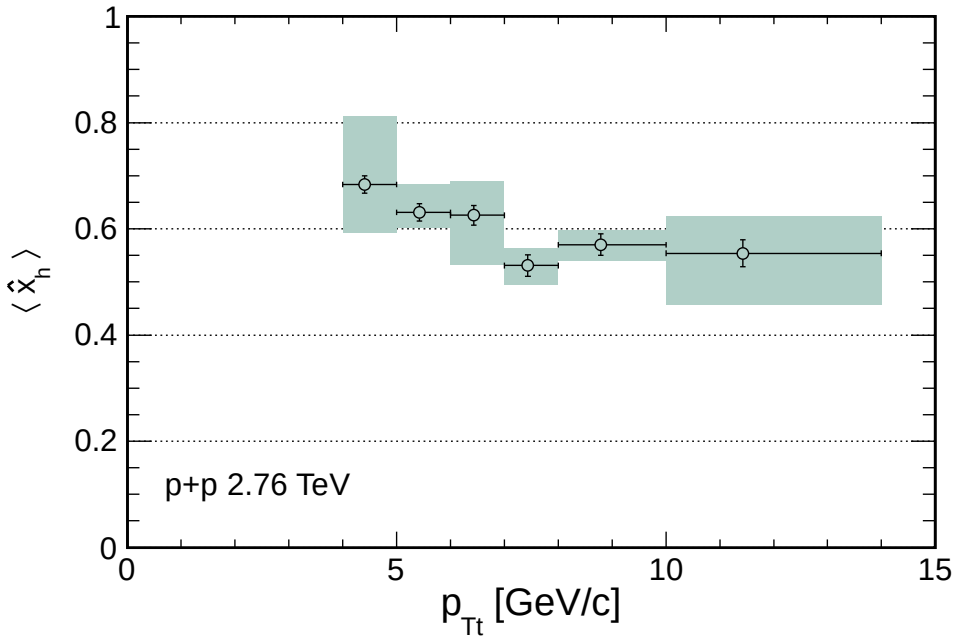

Figure 28: Mean partonic imbalance parameter $\langle \hat{x}_{\mathrm{h}} \rangle$ as a function of p_{Tt}, with 1 GeV $< p_{\mathrm{Ta}} < p_{\mathrm{Tt}}$. The $\langle \hat{x}_{\mathrm{h}} \rangle$ were obtained from the modified Hagedorn function (Eq. (47)) fits to the x_{E} distributions. The grey areas denote systematic errors.

6 Conclusions

I extracted the away side signal distribution of $h^{\pm} - h^{\pm}$ x_{E} in $p+p$ collisions at $\sqrt{s} = 2.76$ TeV from raw distributions measured by ALICE. I then used the signal distributions to study away side fragmentation and momentum imbalance.

I removed the background by calculating the form of the background distribution, normalizing it and then subtracting it from the measured x_{E} distribution. The form I calculated using the Monte Carlo -method, by calculating values of x_{E} by sampling the necessary momentum and angle values from the appropriate distributions. I determined the normalization from the azimuthal correlation function by evaluating the magnitude of the constant part under the correlation peaks. The acquired signal x_{E} distributions rein-

forced the observation made by PHENIX that the x_{E} distributions are not sensitive to the fragmentation function in the case of $h^{\pm} - h^{\pm}$ correlations.

I studied jet imbalance by extracting the partonic imbalance parameter from the x_{E} distributions through a fit. The resulting values suggested that the trigger partons transverse momentum $\hat{p}_{\mathrm{Tt}}$ is always larger than that of the associated partons $\hat{p}_{\mathrm{Ta}}$. This gave clear evidence that this so-called trigger-bias is present already at the partonic level.

The slopes of the tails of the x_{E} distribution have been found to be sensitive to $\langle z_{\mathrm{t}} \rangle = p_{\mathrm{Tt}}/\hat{p}_{\mathrm{Tt}}$. The x_{E} slopes that I acquired were of the same order as those previously measured in ALICE [40], in which they corresponded to $\langle z_{\mathrm{t}} \rangle \sim 0.5$. This gave further evidence that x_{E} distributions at di-hadron correlations do not measure directly the shape of the fragmentation function, but instead the measured values are a convolution over two fragmentation functions - one in trigger side and other away side.

The x_{E} distribution should describe the fragmentation function in the case of isolated $\gamma - h^{\pm}$ correlations. The above analysis done in the case of isolated trigger hadron does indeed result in slopes that are closer to ideal gamma-hadron correlations, where $\langle z_{\mathrm{t}} \rangle \approx 1$. This clearly reflects the increase of the $\langle z_{\mathrm{t}} \rangle$ when the trigger is required to be isolated. The analysis of isolated triggers is not yet performed in the $\sqrt{s} = 2.76$ TeV. Also the gamma-hadron analysis is on-going in ALICE but there are no final results available at the time.

References

[1] L. Evans and P. Bryant, Journal of Instrumentation **3**, S08001.

[2] ATLAS Collaboration, G. Aad *et al.*, (2009), 0901.0512.

[3] The CMS Collaboration, Journal of Physics G: Nuclear and Particle Physics **34**, 995 (2007).

[4] ALICE Collaboration, B. Alessandro *et al.*, Journal of Physics G: Nuclear and Particle Physics **32**, 1295 (2006).

[5] LHCb Collaboration, B. Adeva *et al.*, (2009), 0912.4179.

[6] W. N. Cottingham and D. A. Greenwood, *An Introduction to the Standard Model of Particle Physics*, second ed. (Cambridge University Press, 2007).

[7] R. P. Feynman, *Quantum Electrodynamics* (Westview Press, 1998).

[8] W. Greiner, A. Schäfer, and E. Stein, *Quantum Chromodynamics*, third ed. (Springer, 2007).

[9] Y. L. Dokshitzer, A. H. Mueller, and S. I. Troyan, *Basics of Perturbative QCD* (Editions Frontieres, 1991).

[10] R. K. Ellis, W. J. Stirling, and B. R. Webber, *QCD and Collider Physics* (Cambridge University Press, 1996).

[11] G. Hanson *et al.*, Phys.Rev.Lett. **35**, 1609 (1975).

[12] G. Hanson *et al.*, Phys. Rev. D **26**, 991 (1982).

[13] M. Banner *et al.*, Phys.Lett. **B44**, 537 (1973).

[14] British-Scandinavian ISR Collaboration, B. Alper *et al.*, Phys.Lett. **B44**, 521 (1973).

[15] F. Close, Reports on Progress in Physics **42**, 1285 (1979).

[16] J. C. Collins, D. E. Soper, and G. Sterman, Nucl. Phys. **B263**, 37 (1986).

[17] B. A. Kniehl, G. Kramer, and B. Potter, Nucl.Phys. **B582**, 514 (2000), hep-ph/0010289.

[18] G. Altarelli and G. Parisi, Nucl.Phys. **B126**, 298 (1977).

[19] J. Binnewies, B. A. Kniehl, and G. Kramer, Phys.Rev. **D52**, 4947 (1995), hep-ph/9503464.

[20] TPC/Two Gamma Collaboration, H. Aihara *et al.*, Phys.Rev.Lett. **61**, 1263 (1988).

[21] DELPHI Collaboration, P. Abreu *et al.*, Eur.Phys.J. **C5**, 585 (1998).

[22] ALEPH Collaboration, D. Buskulic *et al.*, Z.Phys. **C66**, 355 (1995).

[23] SLD Collaboration, K. Abe *et al.*, Phys.Rev. **D59**, 052001 (1999), hep-ex/9805029.

[24] OPAL Collaboration, G. Abbiendi *et al.*, Eur.Phys.J. **C11**, 217 (1999), hep-ex/9903027.

[25] ALEPH Collaboration, R. Barate *et al.*, Eur.Phys.J. **C17**, 1 (2000).

[26] R. Sassot, M. Stratmann, and P. Zurita, Phys. Rev. D **81**, 054001 (2010).

[27] M. Cacciari, J. Rojo, G. P. Salam, and G. Soyez, Eur.Phys.J. **C71**, 1539 (2011), 1010.1759.

[28] M. Pratap and J. C. Shaw, Phys. Rev. D **8**, 3938 (1973).

[29] PHENIX, S. S. Adler *et al.*, Phys. Rev. **D74**, 072002 (2006), hep-ex/0605039.

[30] CERN-Columbia-Oxford-Rockefeller Collaboration, CCOR Collaboration, A. Angelis *et al.*, Phys.Scripta **19**, 116 (1979).

[31] R. Feynman, R. Field, and G. Fox, Nucl.Phys. **B128**, 1 (1977).

[32] P. Darriulat, Ann.Rev.Nucl.Part.Sci. **30**, 159 (1980).

[33] M. Jacob, Proceedings EPS International Conferece, Geneva 1979.

[34] PHENIX Collaboration, K. Adcox *et al.*, Nucl.Phys. **A757**, 184 (2005), nucl-ex/0410003.

[35] BRAHMS Collaboration, I. Arsene *et al.*, Nucl.Phys. **A757**, 1 (2005), nucl-ex/0410020.

[36] STAR Collaboration, J. Adams *et al.*, Nucl.Phys. **A757**, 102 (2005), nucl-ex/0501009.

[37] B. Back *et al.*, Nucl.Phys. **A757**, 28 (2005), nucl-ex/0410022.

[38] OPAL Collaboration, G. Alexander *et al.*, Z.Phys. **C69**, 543 (1996).

[39] DELPHI Collaboration, P. Abreu *et al.*, Eur.Phys.J. **C13**, 573 (2000).

[40] ALICE Collaboration, Y. Mao, J.Phys. **G38**, 124094 (2011), 1107.0873.

[41] F. Krizek, (2012), Proceedings 6th International Workshop High-p_T physics at LHC 2011, Utrecht, Netherlands, Apr 2011.

[42] ALICE Collaboration, K. Aamodt *et al.*, Journal of Instrumentation **3**, S08002 (2008).

[43] J. F. Grosse-Oetringhaus, *Measurement of the Charged-Particle Multiplicity in Proton–Proton Collisions with the ALICE Detector*, PhD thesis, University of Münster, 2009.

[44] ALICE Collaboration, K. Aamodt *et al.*, Phys. Rev. D **84**, 112004 (2011).

[45] ALICE Collaboration, B. Abelev *et al.*, Eur. Phys. J. C (2012), 1208.4968.

[46] F. Krizek, J. Rak, D. Kim, J. Kral, and S. S. Räsänen, Run QA, tracking efficiency and acceptance correction in $p+p$ at $\sqrt{s} = 0.9$, 7 TeV 2010 data, ALICE internal note, not published, 2011.

[47] T. Sjostrand, S. Mrenna, and P. Z. Skands, Comput.Phys.Commun. **178**, 852 (2008), 0710.3820.

[48] R. Brun and F. Rademakers, (1996), Proceedings AIHENP'96 Workshop, Lausanne 1996.

[49] R. Brun and F. Rademakers, Nuclear Instruments and Methods in Physics Research A **389**, 81 (1997).

[50] F. Krizek, J. Rak, D. Kim, S. S. Räsänen, and M. Kervinen, Analysis of the longitudinal component of associated particle transverse momentum in $p+p$ at $\sqrt{s} = 0.9$, 2.76 and 7 TeV, ALICE internal note, not published, 2011.

[51] M. Kervinen, (2012), Research report: Extracting the underlying event background from the x_{E} distribution at $\sqrt{s} = 7$ TeV (unpublished).

[52] R. Engel, Phojet manual, program version 1.05c, 1996.

[53] F. Krizek, private communication.

Appendix A

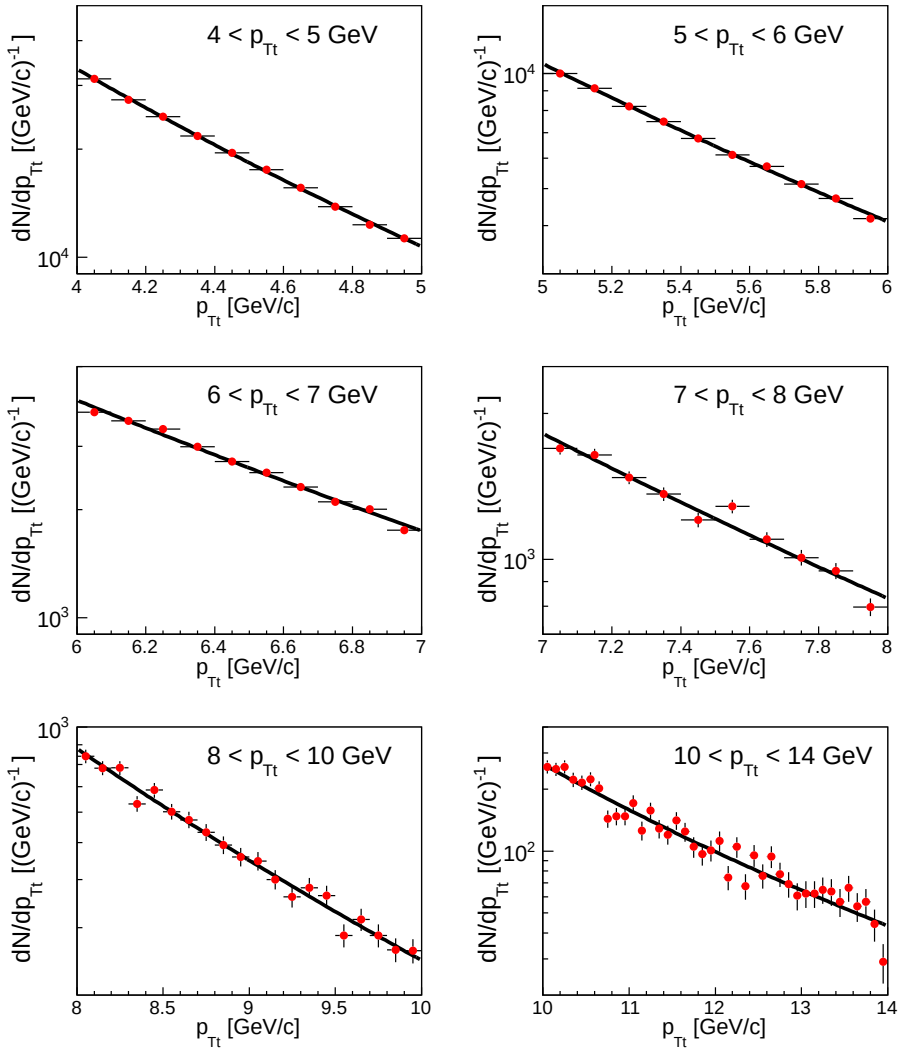

Figure 29: Trigger p_{T} distribution with a power law fit from $p+p$ collisions at $\sqrt{s} = 2.76$ TeV

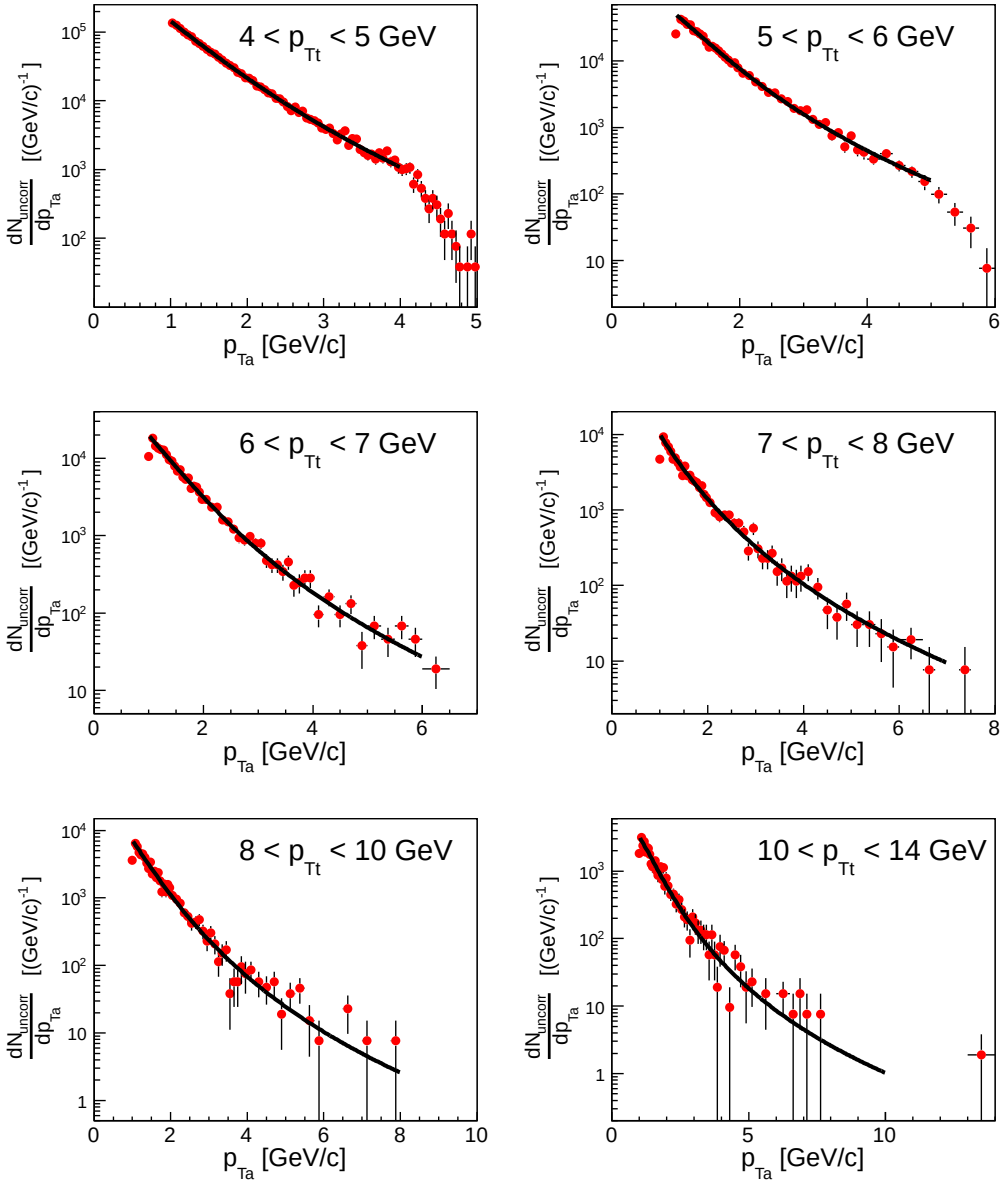

Figure 30: Fit of the Kaplan function to the underlying event p_{Ta} distribution from $p+p$ collisions at $\sqrt{s} = 2.76$ TeV

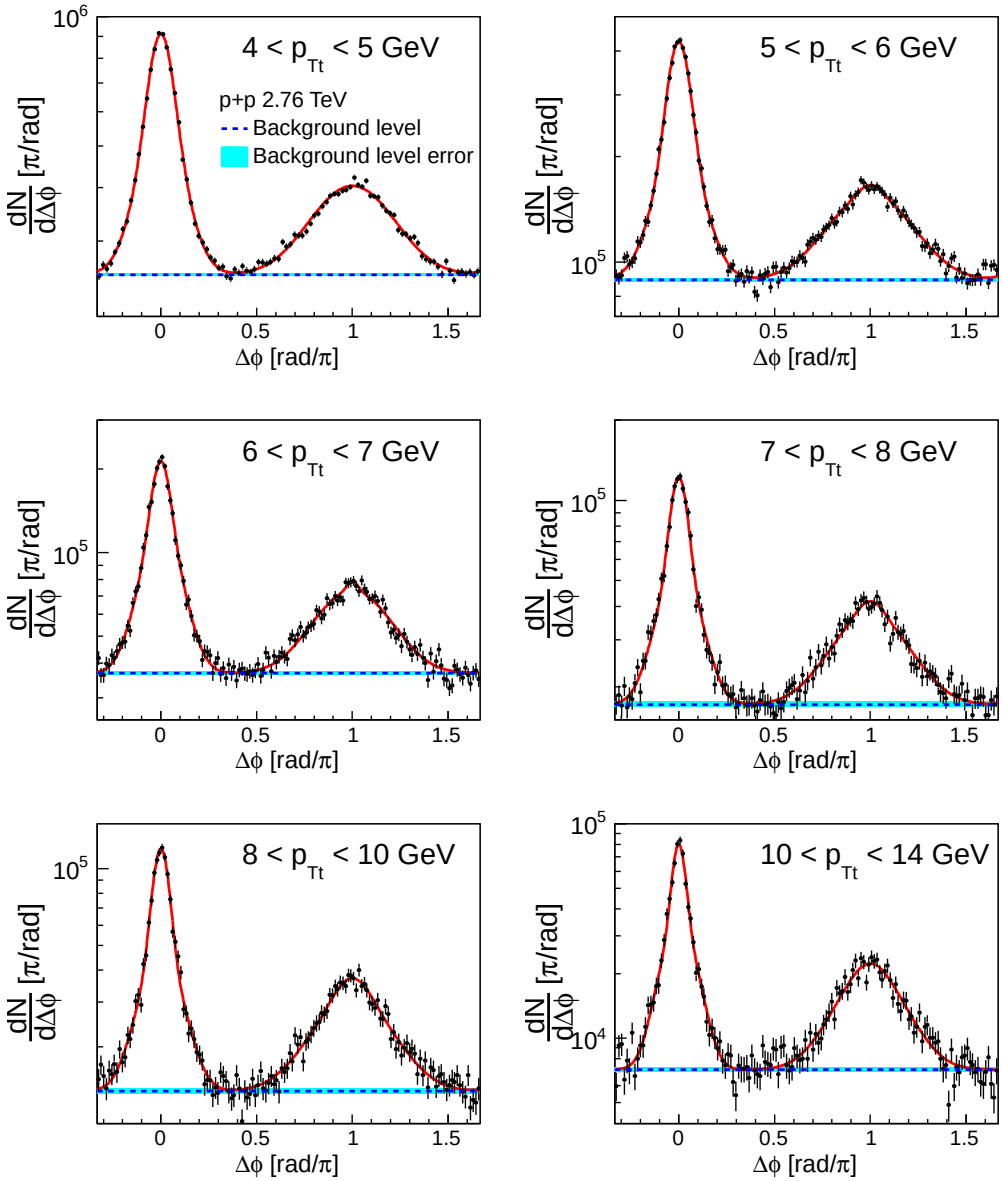

Figure 31: Azimuthal correlation function from $p+p$ collisions at $\sqrt{s} = 2.76$ TeV that have been fit with a function according to Eq. (43) and (45). The blue dashed line represents the underlying event pedestal and the light blue band its error.

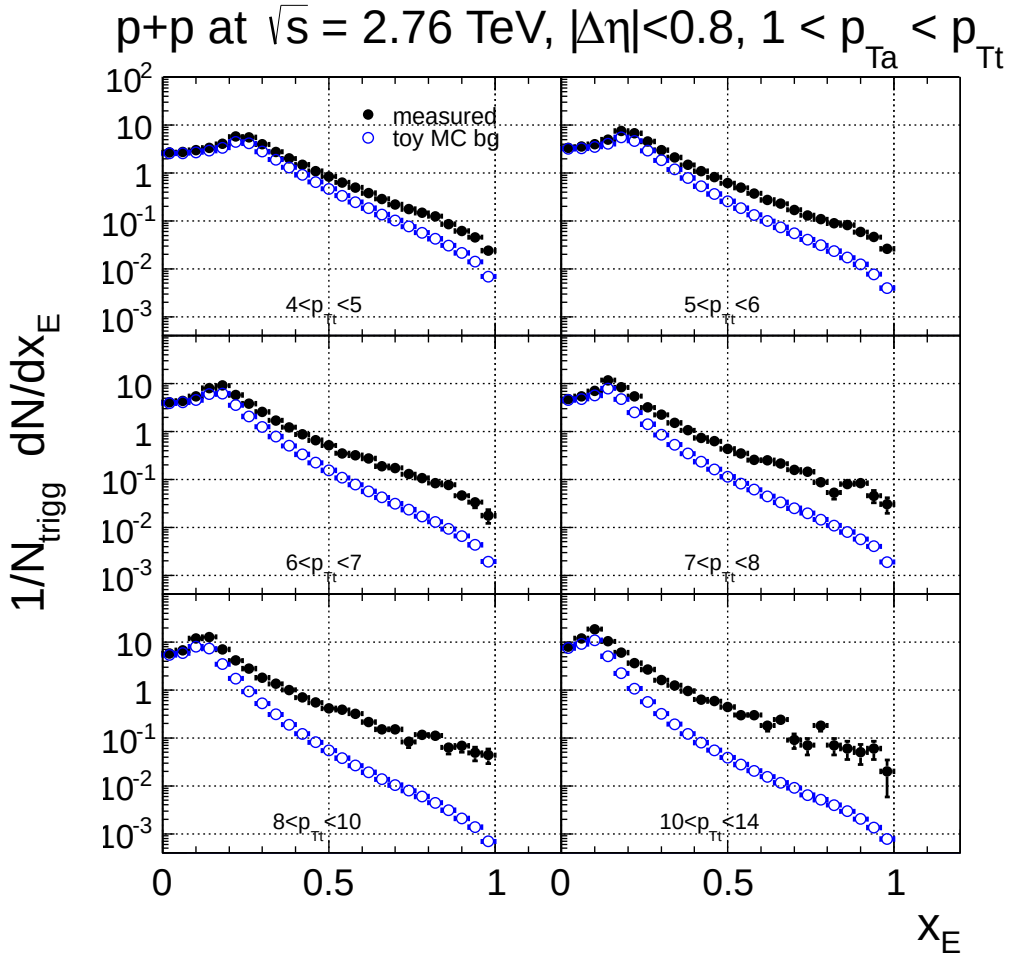

Figure 32: Measured away side x_{E} distribution (solid, black) and the corresponding Monte Carlo -generated background distribution (hollow, blue) from $p+p$ collisions at $\sqrt{s} = 2.76$ TeV and $|\Delta\eta| < 0.8$.

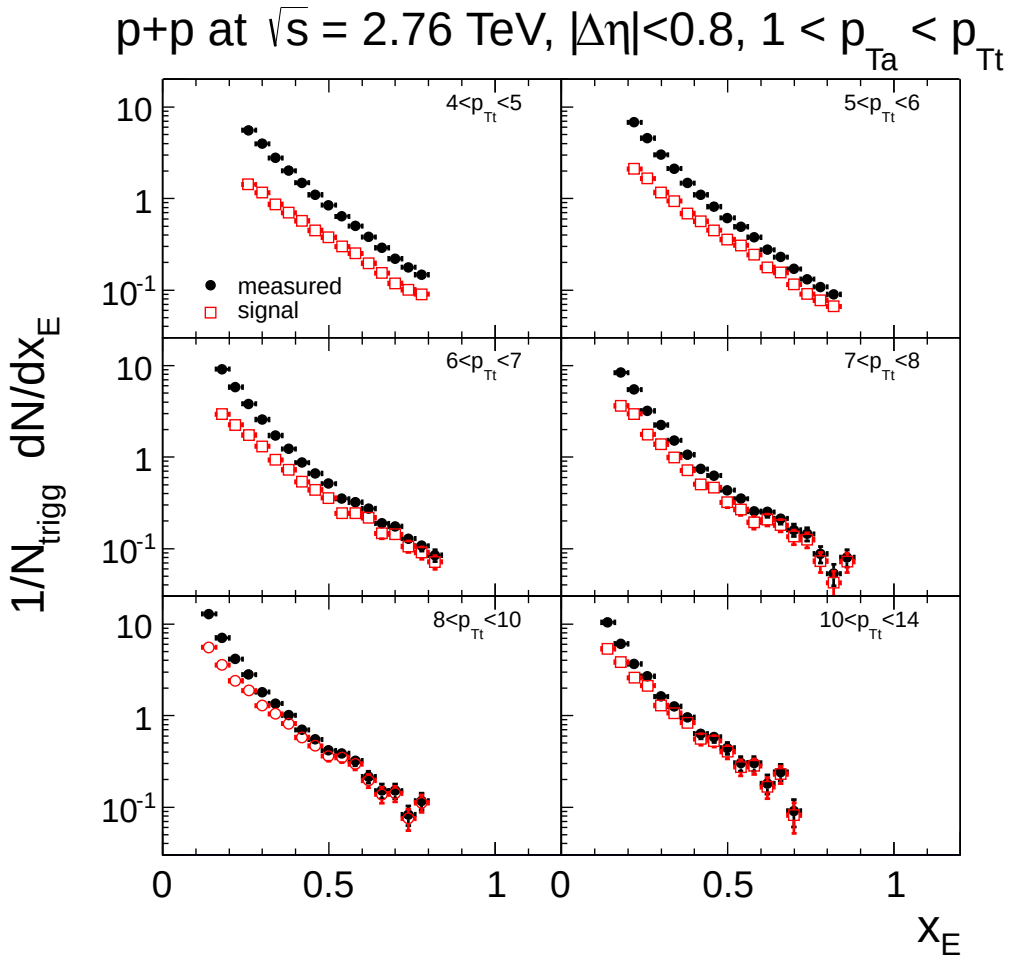

Figure 33: Signal away side x_{E} distribution (hollow, red) and measured x_{E} distribution (solid, black) from $p+p$ collisions at $\sqrt{s} = 2.76$ TeV and $|\Delta\eta| < 0.8$.

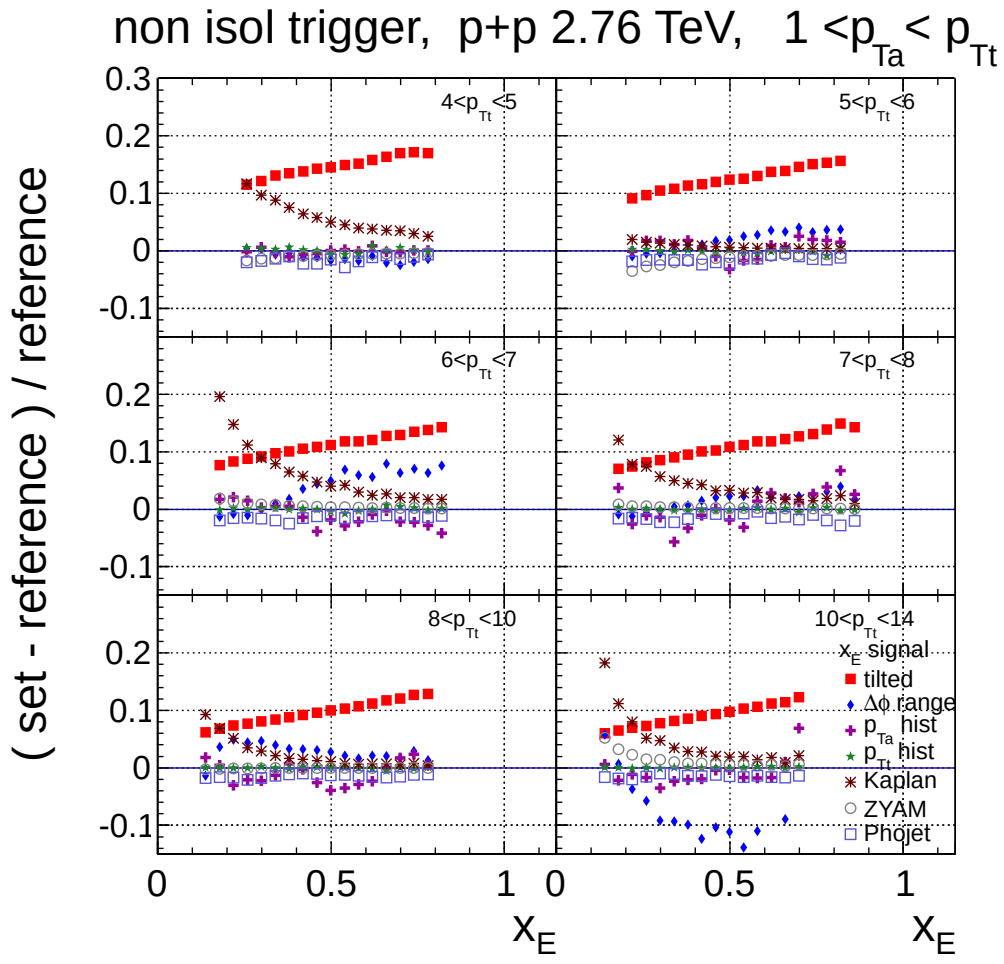

Figure 34: The relative differences of the signal x_{E} distributions between the reference data and each source of systematic error